PHYSICAL REVIEW A VOLUME 39, NUMBER 4 FEBRUARY 15, 1989

Localized transmission of electromagnetic energy

Richard W. Ziolkowski
Engineering Research Division (L-156), Lawrence Livermore National Laboratory, University of California, P.O. Box 5504, Livermore, California 94550
(Received 4 April 1988)

Novel electromagnetic directed-energy pulse train (EDEPT) solutions of Maxwell's equations have been obtained. One particular solution, the modified-power-spectrum (MPS) pulse, will be described in detail. EDEPT's such as the MPS pulses, can be tailored to give localized energy transmission along a specified direction in space that is significantly improved over conventional diffraction-limited beams. Moreover, they represent fields that recover their initial amplitudes along the direction of propagation at extremely large distances from their initial location. These EDEPT solutions are not physically pathological and can be reconstructed from causal Green's functions. In fact, these fields appear to be launchable from finite-aperture antennas.

I. INTRODUCTION

The pioneering work Brittingham[1] first suggested the possibility of solutions of Maxwell's equations that describe efficient, localized transfer of electromagnetic energy in space. It has been recently discovered that these original "focus wave modes" (FWM's) represent Gaussian beams that translate through space with only local deformations.[2-5] Unfortunately, the FWM is not focused in the sense originally intended, i.e., it is not a purely localized, translationally invariant solution of the wave equation. The latter is, in fact, impossible to obtain. A boost solution of the form $\Phi(x,y,z-ct)$ requires $(\Delta-\partial_{ct}^2)\Phi(\mathbf{r}_\perp,z-ct)=\Delta_\perp\Phi=0$ and, hence, that Φ be a harmonic function. This precludes Φ from having a compact spatial support. Moreover, despite having a finite energy density the FWM's have infinite total energy. An attempt at constructing a finite-energy FWM was made by Brittingham in Ref. 1, but his three-region extension was shown to be incorrect by Wu and King.[6] Nonetheless, as explained in Ref. 2 and in Sec. II below, these fundamental Gaussian beams can be used to synthesize other interesting, novel, exact solutions of the wave and Maxwell's equations. These superpositions will be called "electromagnetic directed-energy pulse trains," EDEPT's for short. In contrast to the original FWM's, these EDEPT solutions have finite-energy density *and* finite total energy. It will be shown in Secs. II and III that the EDEPT solutions can be tailored to give localized transmission of electromagnetic energy in space-time.

As a result of Brittingham's work, a number of papers have appeared over the past several years which discuss the possibility of transmitting electromagnetic energy in space in a nonstandard fashion. Besides the EDEPT solutions,[7-10] these have included efforts on "splash modes,"[11,12] "EM missiles,"[13-17] "Bessel beams,"[18-23] "EM bullets,"[24,25] and "transient beams."[9,26-30]

The splash mode was originally introduced in Ref. 2 as the first example of the class of solutions constructed from superpositions of the original FWM's. Hillion has extended the FWM and the splash-mode concepts to the realm of spinors.[11,12] With this approach he is readily able to derive interesting fields and to examine their propagation characteristics. The term splash mode is applied by him in the same manner as the term EDEPT is used here. The latter is preferred in the present context because the pulses developed below achieve directed, localized transmission of energy.

The EM missile concept, recently reported by Wu[13] and others,[14,15] exploits a loophole in the classical $1/r^2$ energy-decay behavior of a field originating from a finite aperture. By increasing the rise time of the excitation pulse in an aperture (hence, the importance of its highest frequencies), one can achieve an energy decay of $1/r^{2\epsilon}$, where $\epsilon\in[0,1]$ is related to the rise time of the pulse. The "missile" thus achieves slower than classical decay over large distances by pushing the classical Fresnel–far-field boundary farther away from the aperture. Recent experiments have actually confirmed this effect.[16] Nonetheless, we may have a practical limitation in realizing the effect over large distances because of our inability to field sources that achieve the necessary pulse rise times.[17]

The Bessel beams are simply eigenmodes of the wave operator and had been described on numerous occasions[18-20] prior to their development in Ref. 21. There, Durnin notes that the Bessel beams are "nondiffracting" in a particular sense and shows via numerical simulations that a finite-aperture approximation to the lowest order field—the J_0 beam—can possess a remarkable depth of field. This effect was realized experimentally,[22,23] at least in the near field of the aperture. This experiment corroborates the fact that one can closely approximate the behavior of a homogeneous-wave-equation solution from a finite aperture. These Bessel beams, like the FWM's, have finite-energy density but infinite energy. It will be shown below that the EDEPT representation can be rewritten in terms of a superposition of these Bessel beams.

Similarly, EM bullets[24] are constructed asymptotically from a representation of solutions of Maxwell's equations based on eigenmodes of the associated curl operators.[25]

A field that decays as $1/r$ and that becomes localized near a specified direction is obtained.

Transient beams, on the other hand, are the projections onto real space of the fields originating from pulsed sources at stationary complex locations. These fields are constructed from analytic continuations of the Green's function of the wave operator to complex space-time. In contrast to the moving complex source description of the fundamental Gaussian pulse given in Ref. 2, these transient beams are constructed by fixing the location of a source at a complex location and by allowing time to be complex as well.[9,26-30] However, as mentioned below, these solutions should be connected directly to the EDEPT solutions through a complex Lorentz transformation.

In this paper it will be shown that EDEPT's can be tailored to give directed transmission of electromagnetic energy in space-time. In particular, pulses will be described that can be designed to give localized energy transmission that is significantly improved over conventional diffraction-limited beams and to recover their initial amplitude along a specified direction of propagation at very large distances from their initial location. In particular, a number of calculations for one of these solutions, the modified-power-spectrum (MPS) pulse, will be presented to support these claims. It will be shown that these MPS pulses exist, that they are not physically pathological, and that a Huygens reconstruction based on a finite planar array of point sources reproduces close approximations to them at large distances away from that array. This reconstruction will be described in detail in Sec. IV; it appears to be insensitive to spatial windowing or frequency filtering and even to adding random Gaussian noise to the array source functions. A summary of the results in this paper and a discussion of what is left for further examination will be given in Sec. V.

The pulses to be described below have very desirable localized wave transmission characteristics which suggest a number of potential applications. These include microscopes with infinite depths of field, low-loss power transmission, secure communications, remote sensing, and directed-energy weapons. On the other hand, even if it transpires that these pulses or their practical applications are not completely realizable, the following solution techniques and the resulting clumplike wave solutions or "macrophotons" have a number of important theoretical applications.

II. SUPERPOSITIONS OF THE FUNDAMENTAL GAUSSIAN PULSES

The fundamental Gaussian pulses can be described as a class of exact solutions of the wave equation that originate from moving complex sources.[2] In particular, if one assumes a solution

$$\Phi_k(\mathbf{r},t)=e^{ik(z+ct)}G(x,y,z-ct) \tag{2.1}$$

of the scalar wave equation in real space,

$$(\Delta-\partial_{ct}^2)\Phi_k(\mathbf{r},t)=0\ , \tag{2.2}$$

the latter reduces to a Schrödinger equation in the pulse center or light cone variable $\tau=z-ct$:

$$(\Delta_\perp+4ik\partial_\tau)G(\mathbf{r}_\perp,\tau)=\delta(\mathbf{r}_\perp)\delta(\tau-iz_0)\ . \tag{2.3}$$

The source term is located at the moving-complex location $(0,0,z=ct+iz_0)$. Let the transverse distance distance $\rho=(\mathbf{r}_\perp\cdot\mathbf{r}_\perp)^{1/2}=(x^2+y^2)^{1/2}$. This equation has the solution

$$G(\mathbf{r}_\perp,\tau)=\frac{e^{-k\rho^2/(z_0+i\tau)}}{4\pi i(z_0+i\tau)}\ . \tag{2.4}$$

Thus the original wave equation (2) has the moving, modified Gaussian pulse

$$\Phi_k(\mathbf{r},t)=e^{ik(z+ct)}\frac{e^{-k\rho^2/V}}{4\pi iV} \tag{2.5}$$

as an *exact* solution. The complex variance $1/V=1/A-i/R$ yields the beam spread $A=z_0+\tau^2/z_0$, the phase front curvature $R=\tau+z_0^2/\tau$, and beam waist $w=(A/k)^{1/2}$. Higher-order pulses can be constructed simply by applying the Hermite or Laguerre polynomial operators to the basic pulse (2.5).[2-4]

If one restricts oneself to real space only, the source term in (2.3) disappears. Its presence simply corroborates our intuition that a field should originate from some source. Physically, we realize the projection of the "moving-complex-center" field (2.5) onto real space-time. It is a solution of the homogeneous equation (2.2) there. This "moving-complex-center wave" represents a generalization of earlier work by Deschamps[31] and Felsen[32] describing "stationary-complex-center waves," i.e., Gaussian beams as fields radiated from stationary complex-source points. Although the concept of a source at a complex location is nonintuitive, it has led to several successful analyses of the propagation and scattering of Gaussian beams in complicated environments.[33-38] As with Gaussian beams, it is a convenient but not always necessary description. In fact, as shown briefly in Appendix A, Eq. (2.5) can be derived from a modified Hermite-Gaussian laser-field analysis without any recourse to the concept of a source at a complex location.

As illustrated in Ref. 2 and in Fig. 1, this fundamental pulse describes a Gaussian beam that translates through space-time with only local variations. Figure 1 shows surface plots and the corresponding contour plots of $\mathrm{Re}[4\pi i\Phi_k(\rho,z,t)]$ with $z_0=1.0$ cm and $k=0.333$ cm^{-1}. These plots depict this quantity relative to the pulse-center locations $z=0.0$ km and $z=9.42\times10^2$ km. Those distances correspond to the times $t=0$ and $t=\pi\times10^{-3}$ sec. Throughout this paper, unless noted otherwise, all field quantities plotted in figures of this type will be normalized to their maximum value at $t=0$ and the direction of propagation will be taken along the positive z axis. These choices do no affect the generality of the results to be discussed below. The transverse space coordinate ρ is measured in centimeters; the longitudinal space coordinate $z-ct$ is the distance in centimeters along the direction of propagation away from the pulse center $z=ct$.

The fundamental Gaussian pulses have several interesting characteristics. First, it is easily seen that (2.5) recovers its initial amplitude at very large distances from its in-

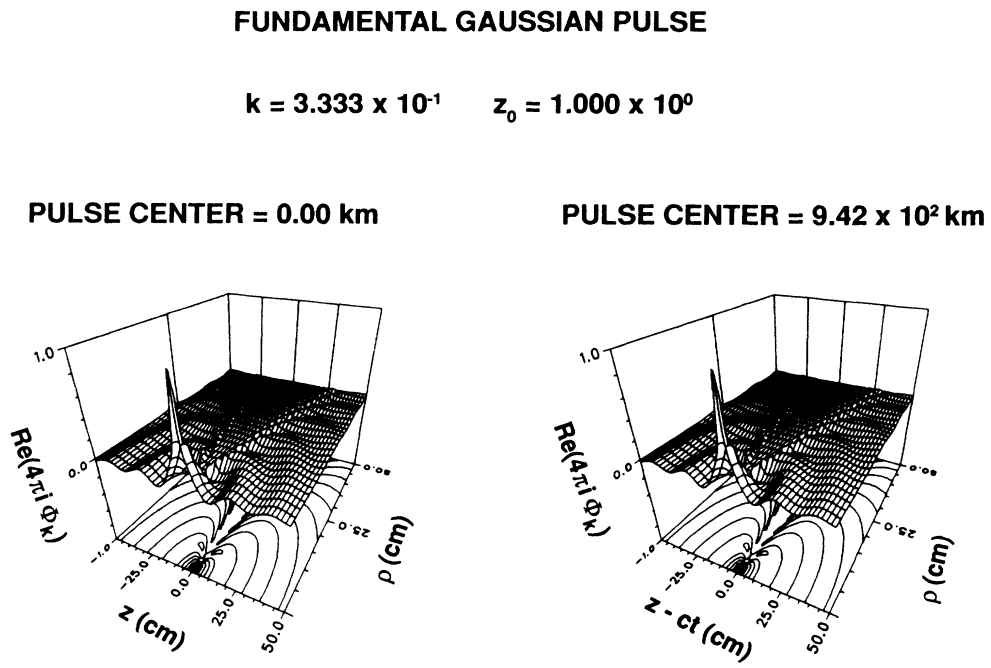

FIG. 1. The exact solution Φ_k is a moving, modified Gaussian pulse. The real part of $4\pi i\Phi_k$ for the parameters $k=0.333\ \text{cm}^{-1}$ and $z_0=1.0$ cm shows the recovery of the initial pulse at a large distance from its initial position.

itial position. In particular,

$$\text{Re}[4\pi i z_0\Phi_k(\rho=0.0,\ z=ct)]=\cos(2kz)\ ,$$

so that its initial amplitude is recovered for every $z=n\pi/k$, n being a positive integer. The times in Fig. 1 were chosen to illustrate this behavior. Secondly, the frequency (ω) spectrum of the Gaussian pulse (2.5) in the transverse plane $z=0$ is unusual and is nonzero only for $\omega>kc$ or $-\omega<-kc$.[4] This means that the backwards-propagating plane wave acts effectively as a high pass filter for frequencies above kc. Next, with z_0 fixed, the pulse becomes more localized with increasing values of k. This effect is illustrated in Figs. 2–4, where $[\text{Re}(4\pi i\Phi_k)]^2$ is plotted. Note that the scales of the axes

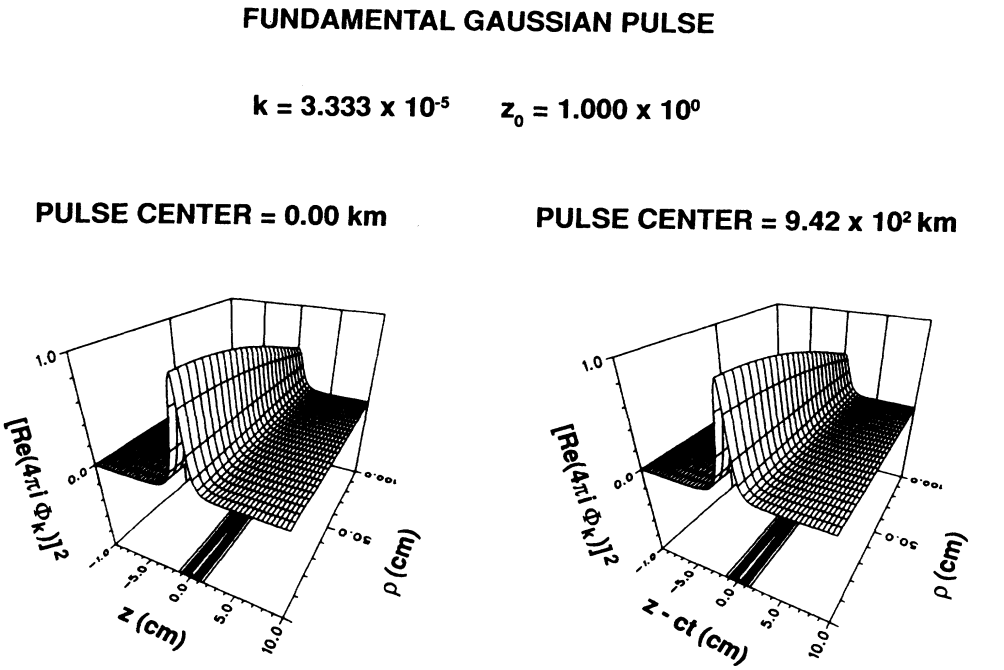

FIG. 2. For small values of k the fundamental Gaussian pulse looks locally like a transverse plane wave. The square of the real part of $4\pi i\Phi_k$ is shown for the parameters $k=3.333\times10^{-5}\ \text{cm}^{-1}$ and $z_0=1.0$ cm.

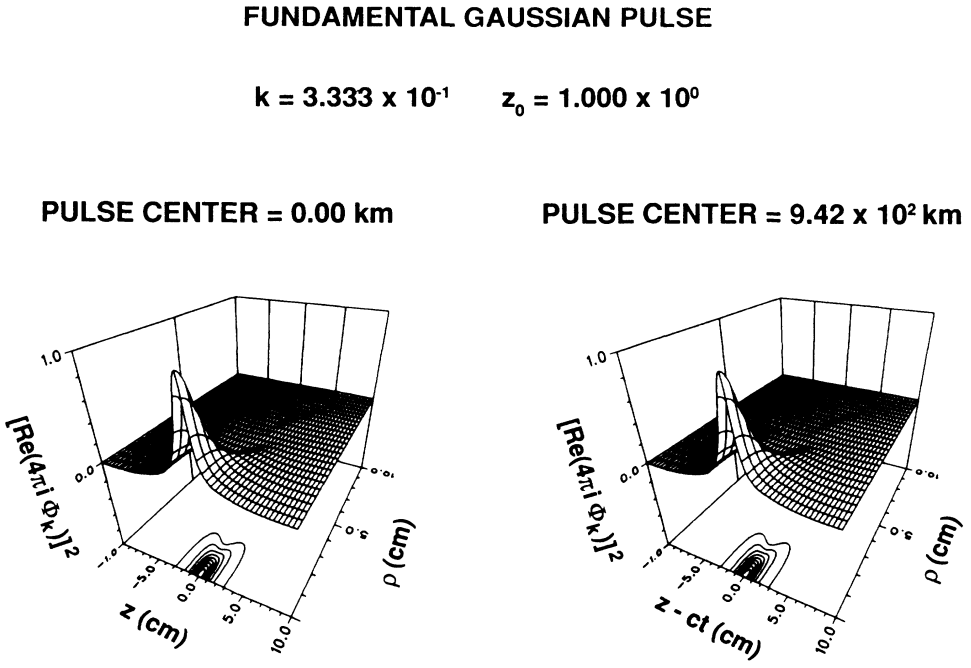

FIG. 3. As k increases, the fundamental Gaussian pulse becomes more localized along the direction of propagation. The square of the real part of $4\pi i\Phi_k$ is shown for the parameters $k=3.333\times10^{-1}$ cm^{-1} and $z_0=1.0$ cm.

have been varied to assure adequate visualization of the major features of this quantity. The parameter k is increased from 3.333×10^{-5} cm^{-1} in Fig. 2 to 0.333 cm^{-1} in Fig. 3 to 3.333 cm^{-1} in Fig. 4. These figures illustrate that for low values of k the fundamental Gaussian pulse looks like a transverse plane wave locally and that for large k it becomes localized near the z axis, the axis of propagation. Finally, for all k the fundamental Gaussian pulses share with plane waves the property of having infinite energy, but finite-energy density. The infinite-

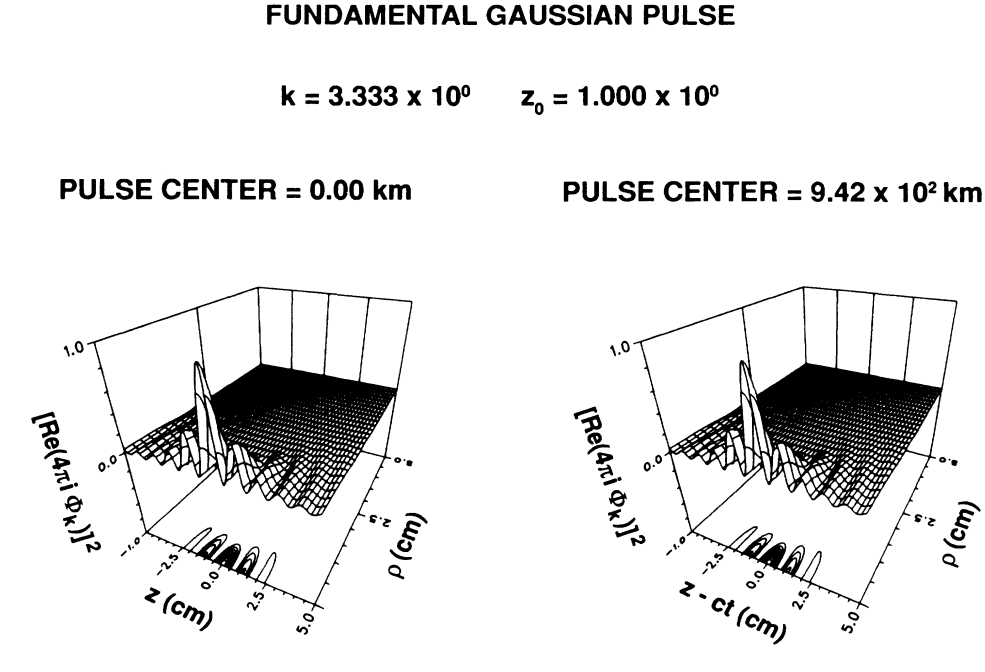

FIG. 4. For large k, the fundamental Gaussian pulse is very localized along the direction of propagation. The square of the real part of $4\pi i\Phi_k$ is shown for the parameters $k=3.333$ cm^{-1} and $z_0=1.0$ cm.

energy results because the variation of the magnitude of (2.5) with respect to the transverse coordinate yields a constant for each partial energy integral over a transverse cross section. However, as with plane waves, this is not to be considered as a drawback *per se*. The ansatz (2.1) has introduced an added degree of freedom into the solution through the variable k that can be exploited. As shown in Ref. 2, these fundamental Gaussian pulses can be used as basis functions to represent new transient solutions of Eq. (2.2).

In particular, the general EDEPT solution

$$f(\mathbf{r},t)=\int_0^\infty \Phi_k(\mathbf{r},t)F(k)dk$$
$$=\frac{1}{4\pi i[z_0+i(z-ct)]}\int_0^\infty dk\, F(k)e^{-ks(\rho,z,t)}\,, \tag{2.6}$$

where

$$s(\rho,z,t)=\frac{\rho^2}{z_0+i(z-ct)}-i(z+ct) \tag{2.7}$$

is an exact source-free solution of the wave equation. As reported in Ref. 2, the superposition with "complex-traveling-center-wave" basis functions, Eq. (2.6), has an inverse. The functions

$$\Psi_k(\rho,\tau,\sigma)=8\pi^{1/2}e^{-(\tau/4kz_0)^2}\Phi_k(\rho,\tau,\sigma)\,,$$

where $\sigma=z+ct$ are biorthogonal to the Φ_k. This means these basis functions satisfy the completeness relation

$$\int_{-\infty}^{\infty}d\sigma\int_{-\infty}^{\infty}d\tau\int_0^\infty d\rho\,\rho\Psi_k^*(\rho,\tau,\sigma)\Psi_{k'}(\rho,\tau,\sigma)$$
$$=\delta(k-k')\,,$$

where Ψ_k^* is the complex conjugate of Ψ_k.

The representation (2.6), in contrast to plane-wave decompositions, utilizes basis functions that are more localized in space and hence, by their very nature, are better suited to described the directed transmission of electromagnetic energy in space. As shown in Appendix B, the EDEPT representation (2.6) yields finite energy solutions of the wave equation (2.2) if $F(k)$ satisfies

$$U_{\text{tot}}=\int_0^\infty dk\,|F(k)|^2e^{2kz_0}E_1(2kz_0)$$
$$<\frac{1}{2z_0}\int_0^\infty dk\,|F(k)|^2\frac{1}{k}<\infty\,, \tag{2.8}$$

where $E_n(x)$ is the exponential integral function of order n. This occurs, for example, if $k^{-1/2}F(k)$ is square integrable. As will be discussed below, the MPS pulse satisfies this requirement. As shown in Appendix B, the original splash pulse discussed in Ref. 2 also has finite energy.

Thus the EDEPT solutions are composed of Gaussian pulses that resemble plane waves as well as localized packets. In interactions with scattering objects they can exhibit either behavior, depending on what portion of the spectrum is affected by the scattering event. Consequently, the EDEPT's are at least a step closer to the unrealized intentions of Brittingham in Ref. 1 of a classical description of a photon, a finite energy solution of Maxwell's equations that exhibits a wave-particle duality.

Notice that a sum over the independent parameter k was chosen rather than one, for example, over the complex source displacement parameter z_0. The choice to superimpose over k was originally a practical one. Even for simple choices of spectra over z_0 the resulting integrals are extremely difficult to calculate. The integrals over k are much less complicated and richer in quantity than the ones over z_0. Many interesting solutions of the wave equation are obtained simply by referring to a Laplace transform table. Combinations of these superpositions are also available in principle. Recently it has also been recognized that the choice of superimposing over k is more fundamental because it is associated with the extra degree of freedom introduced by the ansatz (2.1) and because, as it will be described below, it allows one to mitigate the presence of the backward-propagating plane-wave component.

Also note that the existence of the localized basis functions (2.5) could have been anticipated from earlier studies on complex Lorentz transformations of the wave and Maxwell's equations.[39–41] Trautman's work appears to be the most relevant. He actually mentions (albeit briefly) one Lorentz transformation that, taken in the present context, would lead to the FWM solution. This concept of a complex Lorentz transformation actually connects the present work on moving-complex-source fields with the related work on pulsed, stationary complex sources.[9,26–30]

III. EDEPT SOLUTIONS OF MAXWELL's EQUATIONS

In this section the derivation of the electromagnetic (EM) fields from the localized scalar wave equation solutions will be described. The modified-power-spectrum pulse is introduced and the corresponding EM fields are derived. A number of numerical results are presented to demonstrate that these EDEPT solutions can be tailored to give directed EM energy transfer in space.

A. EM fields from Hertz potentials

Solutions to Maxwell's equations follow naturally from the scalar wave equation solutions. Defining the electric, $\mathbf{\Pi}_e=f\hat{\mathbf{n}}$, or magnetic, $\mathbf{\Pi}_h=f\hat{\mathbf{n}}$, Hertz potential along the arbitrary direction $\hat{\mathbf{n}}$, one readily obtains fields that are TE or TM with respect to $\hat{\mathbf{n}}$. In particular, TE polarization,

$$\mathbf{E}=-Z_0\nabla\times\partial_{ct}\mathbf{\Pi}_h\,,$$
$$\mathbf{H}=\nabla(\nabla\cdot\mathbf{\Pi}_h)-\partial_{ct}^2\mathbf{\Pi}_h\,, \tag{3.1a}$$

TM polarization,

$$\mathbf{E}=\nabla(\nabla\cdot\mathbf{\Pi}_e)-\partial_{ct}^2\mathbf{\Pi}_e\,,$$
$$\mathbf{H}=+Y_0\nabla\times\partial_{ct}\mathbf{\Pi}_e\,, \tag{3.1b}$$

where $Z_0=\sqrt{\mu_0/\epsilon_0}$ and $Y_0=\sqrt{\epsilon_0/\mu_0}$ are, respectively, the free-space impedance and admittance. For instance, if $n=\hat{\mathbf{z}}$, then the TE field components are given by the expressions

$$
\begin{aligned}
E_r &= -Z_0 \frac{1}{r} \partial_\theta \partial_{ct} f \ , \\
E_\theta &= +Z_0 \partial_r \partial_{ct} f \ , \\
E_z &= 0 \ , \\
H_r &= +\partial_r \partial_z f \ , \\
H_\theta &= +\frac{1}{r} \partial_\theta \partial_z f \ , \\
H_z &= (\partial_z^2 - \partial_{ct}^2) f \ .
\end{aligned} \tag{3.1c}
$$

As shown in Appendix B, the total energy of an electromagnetic EDEPT is

$$
\begin{aligned}
U_{\mathrm{EM}} &= \int_{-\infty}^{\infty} dz \int_0^{\infty} d\rho \rho \int_0^{2\pi} d\theta (\epsilon |E_\theta|^2 + \mu |H_\rho|^2 \\
&\quad + \mu |H_z|^2) \\
&= \frac{1}{4 z_0^4} \int_0^{\infty} dk \, |F(k)|^2 [k z_0 + (k z_0)^2] \ .
\end{aligned} \tag{3.2}
$$

Thus an EDEPT will have finite energy, for example, if the spectrum $kF(k)$ is square integrable. A similar finite-energy analysis of a related class of EDEPT's was given by Hillion in Ref. 12.

B. Modified-power-spectrum pulse

Clearly, different spectra $F(k)$ in Eq. (2.6) lead to different wave equation solutions, and hence, to different solutions of Maxwell's equations. As noted above, many interesting solutions of the wave equation are created simply by referring to a Laplace transform table. One particularly interesting spectrum selection is the modified power spectrum:

$$
F(k) = \begin{cases} 4\pi i \beta \dfrac{(\beta k - b)^{\alpha - 1} e^{-a(\beta k - b)}}{\Gamma(\alpha)} \ , & k > \dfrac{b}{\beta} \qquad (3.3a) \\ 0 \ , & 0 \le k < \dfrac{b}{\beta} \ . \qquad (3.3b) \end{cases}
$$

It is so named because it is derived from the power spectrum $F(k) = k^{\alpha - 1} e^{-ak}$ by a scaling and a truncation. In particular, if the Laplace transform is defined as

$$
H(s) \equiv F[h(t)] = \int_0^{\infty} e^{-st} h(t) dt \ ,
$$

the scaling and truncated translation rules

$$
F[h(\beta t)] = \frac{1}{\beta} H(s/\beta) \quad \text{for } \beta > 0 \ ,
$$

$$
F[\chi_b(t) h(t - b)] = e^{-bs} H(s) \quad \text{for } b > 0
$$

lead to the expression

$$
F[\chi_{b/\beta}(t) h(t - b/\beta)] = e^{-bs/\beta} H(s/\beta) \ .
$$

The choice of spectrum (3.3) produces the modified-power-spectrum pulse

$$
f(\mathbf{r}, t) = \frac{1}{z_0 + i(z - ct)} \frac{1}{(s/\beta + a)^{\alpha}} e^{-bs/\beta} \ . \tag{3.4}
$$

Much effort has been concentrated on this MPS pulse because it has an appealing analytical form and its pulse shape can be tailored to a particular application with a straightforward change in parameters. Other spectra, such as those resulting in Laplace transforms involving a term such as $(s^2 + a^2)^{-\nu}$ were avoided because they have a singularity in real space where $s^2 + a^2 = 0$, i.e., where $\rho = 0$ and $\sigma = \pm a$. Similarly, those involving simply the term $s^{-\nu}$ were also avoided because they gave Laplace transforms that have a singularity in real space where $(\rho = 0, \sigma = 0)$.

For a particular choice of spectral parameters, this EDEPT solution has the desired characteristics of localization near the direction of propagation for very large distances. First, the presence of the backward-propagating plane-wave portion of the original focus wave modes (1.5) has been shown in Ref. 29 to lead to some physically pathological properties in that solution. However, by "tweaking" the spectrum; in particular, by setting β to be very large, one can mitigate the effects of these components. The resulting EDEPT pulses, as will be discussed below, are not physically pathological.

Figure 5 shows surface plots and the corresponding contour plots of one such "optimized" MPS field. These plots depict the real part of (3.4) relative to the pulse center locations $z = 0.0$ km and $z = 9.42 \times 10^2$ km, which correspond to the times $t = 0$ and $t = \pi \times 10^{-3}$ sec. The parameters of this particular MPS pulse are $a = 1.0$ cm, $\alpha = 1.0$, $b = 1.0 \times 10^{10}$ cm^{-1}, $\beta = 6.0 \times 10^{15}$, and $z_0 = 1.667 \times 10^{-3}$ cm. The transverse space coordinate ρ is measured in centimeters; the longitudinal space coordinate $z - ct$ is the distance in centimeters along the direction of propagation away from the pulse center $z = ct$. The time history of this particular MPS pulse at $\rho = 0.0$, $z = 1.0$ cm is given in Fig. 6. It is centered about the time $t = z/c$. The corresponding Fourier spectrum is shown in Fig. 7. It is flat at the lower frequencies from dc to about 30.0 GHz, and begins to roll off quickly beginning at about 200.0 GHz, reaching zero around 10^4 GHz.

The behavior of a MPS pulse along the direction of propagation is easily characterized. Let $\beta \gg 1$ and $\alpha = 1$. This corresponds to the case given in Fig. 5. One has

$$
f(\rho = 0, z = ct) = \frac{\cos(2bz/\beta) - (2z/\beta a)\sin(2bz/\beta)}{1 + (2z/\beta a)^2} \frac{1}{a z_0}
$$

$$
\sim \begin{cases} \dfrac{1}{a z_0} \quad \text{when } 2bz/\beta \ll 1 \text{ and } 2z/\beta a < 1 \ , & (3.5a) \\ \cos(2bz/\beta)/a z_0 \quad \text{when } 2z/\beta a < 1 \ , & (3.5b) \\ [\sin(2bz/\beta)/(2z_0/\beta)](1/z) \quad \text{when } 2z/\beta a > 1 \ . & (3.5c) \end{cases}
$$

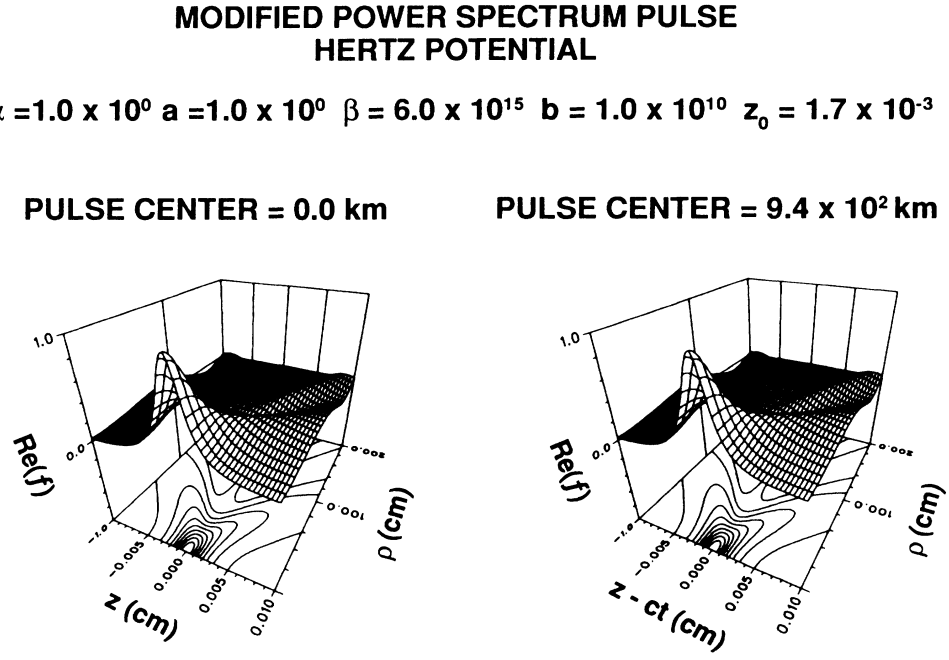

FIG. 5. The modified-power-spectrum pulse is localized along the direction of propagation and recovers its initial amplitude at large distances. The real part of the MPS pulse is shown for the parameters $a=1.0$ cm, $\alpha=1.0$, $b=1.0\times10^{10}$ cm^{-1}, $\beta=6.0\times10^{15}$, and $z_0=1.667\times10^{-3}$ cm.

For a distance $z \ll \beta/2b$ and $z < \beta a/2$, the amplitude of the pulse at the pulse center is constant. It then becomes oscillatory with an oscillation length of $\pi\beta/b$ in an intermediate zone $\beta/2b < z < \beta a/2$, recovering its original amplitude when $z = n(\pi\beta/b)$, n being any positive integer. As will be shown below, the absence of a peak at the pulse center occurs in conjunction with peaks appearing on both sides of the pulse center. Finally, when the observation point is very far away from the origin, $z > \beta a/2$, the MPS pulse decays like $1/z$. The corresponding electromagnetic MPS pulse consequently satisfies the radiation condition at infinity. Notice that when $\beta \gg 1$, different choices of α have little effect on the pulse behavior until this far zone is reached.

The transverse behavior of this MPS pulse at the pulse center is essentially

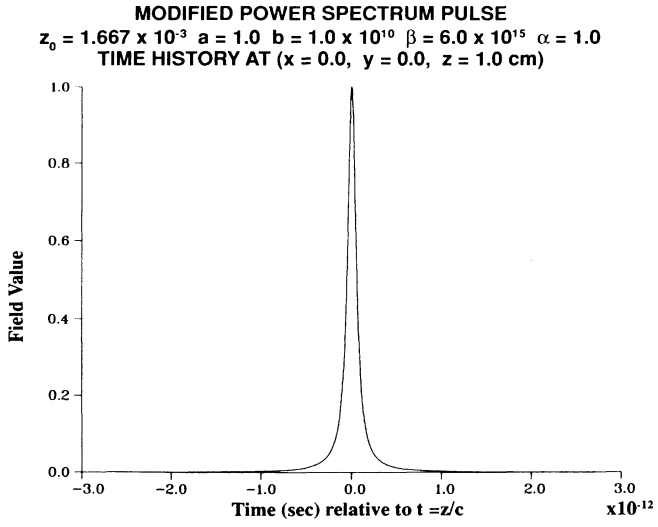

FIG. 6. The time history of the modified-power-spectrum pulse shown in Fig. 5 is given for the point $\rho=0.0$, $z=1.0$ cm.

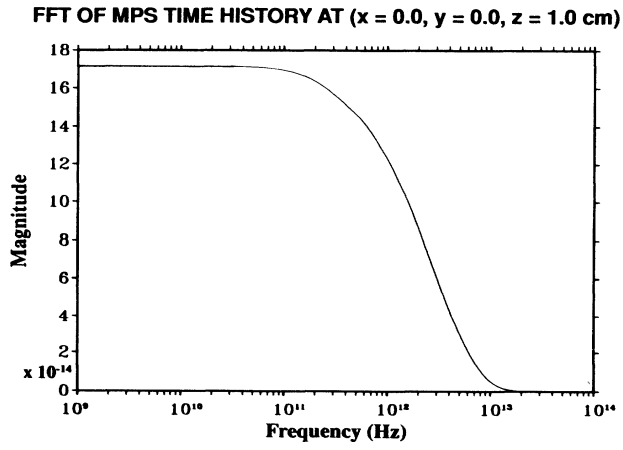

FIG. 7. The Fourier transform of the time history in Fig. 6 shows the pulse spectrum decaying to zero at approximately 1.0×10^{13} Hz.

$$f(\rho, z=ct) \sim e^{-b\rho^2/\beta z_0} f(\rho=0, z=ct) , \tag{3.6}$$

the waist of the Gaussian (the $1/e$ folding point) being $w_0=(b/\beta z_0)^{-1/2}$. Along the direction of propagation z and away from the pulse center the MPS pulse decays as $f \sim 1/[z_0^2+(z-ct)^2]$. Hence it is localized along the direction of propagation as well.

The physical characteristics of the MPS pulse are very appealing. The initial amplitude of the MPS pulse is recovered until the distance $z \sim \beta a/2$; and since β is a free parameter, this distance can be made arbitrarily large. Moreover, by adjusting the ratio $b/\beta z_0$, one can adjust the degree of localization along the direction of propagation. For the case in Fig. 5 the value at pulse center remains constant until about $z \sim \beta/2b = 1.0\times 10^5$ cm, where it begins to oscillate, recovering its initial amplitude every $\Delta z = 1.88\times 10^6$ cm until $z \sim \beta a/2 = 3.0\times 10^{15}$ cm, where the $1/z$ behavior begins to dominate. The $1/e$ point of the amplitude of the pulse in the pulse center cross section $z=ct$ is $\rho = w_0 = 31.6$ cm. It has also been shown[10] that the transverse spatial spectrum, i.e., the $k_x - k_y$ spectrum, remains nearly invariant as it propagates. Moreover, the transverse spectrum is within the visible region of the allowed transverse wave numbers.

The MPS pulse has finite energy. With (2.8) or (B7) it is easy to show that

$$\begin{aligned} U_{\text{tot}}^{\text{MPS}} &= 4\pi^2\beta^2 e^{2ba} \int_{b/\beta}^{\infty} dk\, e^{-2(\beta a - z_0)k} E_1(2kz_0) \\ &\le \frac{4\pi^2\beta^2}{2z_0} e^{2ba} E_1(2ba) \\ &\le \frac{\pi^2\beta^2}{z_0 ba} \\ &= (\pi w_0^2)(\beta a/2)[2\pi |f(\rho=0, z=0, t=0)|^2] . \end{aligned} \tag{3.7}$$

Thus the energy of the MPS scalar field is essentially contained within the cylindrical volume defined by the Gaussian waist w_0 and the effective propagation length $\beta a/2$.

A number of concerns about the causal nature of the original focus wave mode have been raised in Ref. 29. As mentioned above, the "tweaked" MPS pulse should not suffer from the same pathologies. This can in fact be demonstrated analytically.[42] Briefly, a bidirectional traveling-wave representation of exact solutions of the scalar wave equation (such as the MPS pulse) has been developed, from which a forward- and backward-propagating plane-wave representation can be extracted. In particular, it has been shown that the MPS pulse can be written as

$$f(\mathbf{r},t) = \frac{1}{2\pi} \sum_{n=-\infty}^{\infty} \int_0^{\infty} du \int_0^{\infty} dv \int_0^{\infty} d\chi\, \chi J_n(\chi\rho) e^{in\phi} \delta(uv - \chi^2/4) G_n(u,v;\chi) e^{+iv\sigma} e^{-iu\tau} . \tag{3.8}$$

This is actually a generalization of the EDEPT representation (2.6). The latter is obtained by taking the lowest-order azimuthal mode, introducing the spectrum

$$G_0(u,v;\chi) = \frac{F(v) e^{-uz_0}}{8\pi i} , \tag{3.9}$$

and identifying the parameters v with k. Furthermore, by introducing the variables $\kappa = u - v$ and $\omega = (u+v)c$ into (3.8), the basis functions

$$J_n(\chi\rho) e^{in\phi} e^{+iv\sigma} e^{-iu\tau} \rightarrow J_n(\chi\rho) e^{in\phi} e^{-i(\kappa z - \omega t)} ,$$

the constraint relation $uv = \chi^2/4 \rightarrow \omega^2 = (\kappa^2+\chi^2)c^2$, and the representation (3.8) becomes

$$\begin{aligned} f(\mathbf{r},t) = \frac{1}{\pi} \sum_{n=-\infty}^{\infty} \int_{-\infty}^{\infty} d(\kappa c) \int_0^{\infty} d\omega \int_0^{\infty} d\chi\, \chi J_n(\chi\rho) e^{in\phi} \delta(\omega^2 - (\kappa^2+\chi^2)c^2) \\ \times G_n((\omega+\kappa c)/2c\ ,\ (\omega-\kappa c)/2c\ ;\ \chi) e^{-i(\kappa z - \omega t)} , \end{aligned} \tag{3.10}$$

a superposition of forward- and backward-propagating Bessel beams. Consequently, one can connect (3.8) with a conventional backward- and forward-propagating plane-wave representation

$$\begin{aligned} f(\mathbf{r},t) = \frac{1}{2\pi} \sum_{n=-\infty}^{\infty} \int_0^{\infty} d\kappa \int_0^{\infty} d\omega \int_0^{\infty} d\chi\, \chi J_n(\chi\rho) e^{in\phi} \delta(\omega^2 - (\kappa^2+\chi^2)c^2) \\ \times [G_n^+(\omega,\kappa;\chi) e^{-i(\kappa z - \omega t)} + G_n^-(\omega,\kappa;\chi) e^{+i(\kappa z + \omega t)}] = f_z^+(\mathbf{r},t) + f_z^-(\mathbf{r},t) . \end{aligned} \tag{3.11}$$

In particular, by integrating over ω to remove the δ-function constraint in the lowest-order form of the azimuthally symmetric version of (3.10), we can recover the MPS pulse from the expression

$$f(\mathbf{r},t) = \int_0^{\infty} d\chi\, \chi J_0(\chi\rho) \int_{-\infty}^{\infty} dk_z\, A(\chi, k_z) e^{-i(k_z z - \omega t)} , \tag{3.12}$$

where $\omega = +(\chi^2+k_z^2)^{1/2}c$ and the Fourier spectrum corresponding to the "bidirectional" spectrum " given in (3.9),

$$A(\chi,k_z)=\begin{cases}\dfrac{1}{2\pi}\dfrac{\beta}{\Gamma(\alpha)(\chi^2+k_z^2)^{1/2}}\left[\dfrac{\beta}{2}[(\chi^2+k_z^2)^{1/2}-k_z]-b\right]^{\alpha-1}e^{ba}\exp\{-[(\chi^2+k_z^2)^{1/2}+k_z]z_0/2\} & \\ \qquad\times\exp\{-[(\chi^2+k_z^2)^{1/2}-k_z]\beta a/2\} \quad \text{for } k_z<\dfrac{\beta}{b}\dfrac{\chi^2}{4}-\dfrac{b}{\beta} & (3.13a)\\ 0 \quad \text{for } k_z>\dfrac{\beta}{b}\dfrac{\chi^2}{4}-\dfrac{b}{\beta}\,. & (3.13b)\end{cases}$$

This gives the forward- and backward-propagating forms

$$\begin{aligned}f_z^{+}(\mathbf{r},t)&=\int_{2b/\beta}^{\infty}d\chi\,\chi J_0(\chi\rho)\int_0^{\beta\chi^2/4b-b/\beta}dk_z\;A(\chi,k_z)e^{-i(k_zz-\omega t)}\,,\\ f_z^{-}(\mathbf{r},t)&=\int_0^{2b/\beta}d\chi\,\chi J_0(\chi\rho)\int_{b/\beta-\beta\chi^2/4b}^{\infty}dk_z\;A(\chi,-k_z)e^{+i(k_zz+\omega t)}\\ &\quad+\int_{2b/\beta}^{\infty}d\chi\,\chi J_0(\chi\rho)\int_0^{\infty}dk_z\;A(\chi,-k_z)e^{+i(k_zz+\omega t)}\,.\end{aligned}\tag{3.14}$$

For any value of b/β the ratio of the spectra $A(\chi,+k_z)$ and $A(\chi,-k_z)$ is such that

$$\frac{A(\chi,+k_z)}{A(\chi,-k_z)}\sim e^{|k_z|(\beta a-z_0)}\,.$$

Therefore, for the "tweaked" MPS pulse considered above where $\beta\gg1$, one has $A(\chi,+k_z)\gg A(\chi,-k_z)$ for non-negligible k_z, and hence only the forward propagating component contributes to the MPS pulse. On the other hand, if $\alpha=\beta=1.0$, $b=0$, and $a=z_0$, one recovers the splash pulse reported in Ref. 2 from the MPS pulse. For that case this ratio yields $A(\chi,+k_z)\sim A(\chi,-k_z)$, i.e., there are about equal amounts of forward- and backward-propagating waves. This result is confirmed by Fig. 3 of Ref. 2. The same analysis applied to the focus wave mode reproduces the conclusions reached in Ref. 29.

Therefore, in summary, *the MPS pulse can be designed to recover its initial amplitude after propagating very large distances while remaining localized very near the direction of propagation.* It translates nearly invariantly in the "near" zone, begins to "slosh" about the pulse center in the "intermediate" zone recovering its initial amplitude out to very large distances, and finally begins to fall off as the inverse of the distance from its initial position in the "far" zone. Moreover, it is not physically pathological; its constituents have finite energy, and they are causal and forward propagating.

C. Electromagnetic MPS pulse field derivation

The corresponding electromagnetic fields follow immediately from the Hertz potential formulas (3.1). For brevity, only the TE field will be considered. Because the MPS pulse is axisymmetric, the field consists only of the E_θ, H_r, and H_z field components and Eq. (3.1c) gives

$$E_\theta=+Z_0\partial_r\partial_{ct}f\,,\tag{3.15a}$$

$$H_r=\partial_r\partial_z f\,,\tag{3.15b}$$

$$H_z=(\partial_z^2-\partial_{ct}^2)f\,.\tag{3.15c}$$

The resulting Poynting flux is

$$\mathbf{P}=(E_\theta H_z)\hat{\mathbf{r}}+(-E_\theta H_r)\hat{\mathbf{z}}\,.\tag{3.16}$$

Explicitly, the MPS-field components are given by the expressions

$$E_\theta=+Z_0\partial_{ct}\partial_r f=Z_0\left\{-\frac{1}{\beta}\left[b+\frac{\alpha}{s/\beta+a}\right]\left[\frac{i}{z_0+i\tau}\partial_r s+\partial_{ct}\partial_r s\right]+\frac{1}{\beta^2}\left[\left[b+\frac{\alpha}{s/\beta+a}\right]^2+\frac{\alpha}{(s/\beta+a)^2}\right]\partial_{ct}s\,\partial_r s\right\}f\,,\tag{3.17a}$$

$$H_r=+\partial_z\partial_r f=\left\{+\frac{1}{\beta}\left[b+\frac{\alpha}{s/\beta+a}\right]\left[\frac{i}{z_0+i\tau}\partial_r s-\partial_z\partial_r s\right]+\frac{1}{\beta^2}\left[\left[b+\frac{\alpha}{s/\beta+a}\right]^2+\frac{\alpha}{(s/\beta+a)^2}\right]\partial_z s\,\partial_r s\right\}f\,,\tag{3.17b}$$

$$H_z=+(\partial_z^2-\partial_{ct}^2)f=\left[\frac{1}{\beta^2}\frac{\alpha}{(s/\beta+a)^2}[(\partial_z s)^2-(\partial_{ct}s)^2]-\frac{1}{\beta}\left[b+\frac{\alpha}{s/\beta+a}\right](\partial_z^2 s-\partial_{ct}^2 s)+\frac{1}{\beta^2}\left[b+\frac{\alpha}{s/\beta+a}\right]^2[(\partial_z s)^2-(\partial_{ct}s)^2]+\frac{2i}{\beta(z_0+i\tau)}\left[b+\frac{\alpha}{s/\beta+a}\right](\partial_z s+\partial_{ct}s)\right]f\,.\tag{3.17c}$$

The terms

$$\partial_r s = +\frac{2r}{z_0+i\tau} ,$$

$$\partial_z s = -i\left[\frac{r^2}{(z_0+i\tau)^2}+1\right] ,$$

$$\partial_{ct} s = +i\left[\frac{r^2}{(z_0+i\tau)^2}-1\right] ,$$

$$\partial_z^2 s = -\frac{2r^2}{(z_0+i\tau)^3} ,$$

$$\partial_{ct}^2 s = -\frac{2r^2}{(z_0+i\tau)^3} ,$$

$$\partial_r\partial_z s = -\frac{2ir}{(z_0+i\tau)^2} ,$$

$$\partial_r\partial_{ct} s = +\frac{2ir}{(z_0+i\tau)^2} ,$$

$$(\partial_z s)^2 = -\left[\left[\frac{r^2}{(z_0+i\tau)^2}\right]^2+\frac{2r^2}{(z_0+i\tau)^2}+1\right] ,$$

$$(\partial_{ct} s)^2 = -\left[\left[\frac{r^2}{(z_0+i\tau)^2}\right]^2-\frac{2r^2}{(z_0+i\tau)^2}+1\right] .$$

This gives

$$(\partial_z s)^2-(\partial_{ct} s)^2 = -\frac{4r^2}{(z_0+i\tau)^3} ,$$

$$\partial_z^2 s-\partial_{ct}^2 = 0 ,$$

$$\partial_z s+\partial_{ct} s = -2i ,$$

thus reducing the expression for H_z to

$$H_z = \left[-\frac{4\alpha r^2}{\beta^2(s/\beta+a)^2}\frac{1}{(z_0+i\tau)^2}-\frac{4r^2}{\beta^2}\left[b+\frac{\alpha}{s/\beta+a}\right]^2\frac{1}{(z_0+i\tau)^3}+\frac{4}{\beta(z_0+i\tau)}\left[b+\frac{\alpha}{s/\beta+a}\right]\right]f . \tag{3.17c'}$$

With the expression (3.2) and the MPS spectrum (3.3), the total energy in a MPS EDEPT, as shown in Appendix B, is

$$U_{\mathrm{EM}}^{MPS} = \frac{\pi^2}{z_0^4\beta a^3}[1+2ba+2(ba)^2] . \tag{3.18}$$

In the following results the parameter b is chosen so that $ba \gg 1$. In this case the energy (3.18) becomes

$$U_{\mathrm{EM}}^{\mathrm{MPS}} \sim \frac{2\pi^2 b^2}{z_0^4\beta a} \sim (\pi w_0^2)(\beta a/2)[2\pi|E_\theta^{\max}(z=0,\, t=0)|^2]\left[\frac{b}{\beta}\right]^2 , \tag{3.18'}$$

where $E_\theta^{\max}(z=0,\, t=0)$ is the maximum value of E_θ at $t=0$ in the initial plane $z=0$. Thus, as in the scalar field case, this energy is contained in the effective cylindrical volume $(\pi w_0^2)(\beta a/2)$. It is additionally modified by the inverse square of the oscillation frequency, $(\beta\pi/b)^{-2}$, connected with the intermediate zone.

D. Modified-power-spectrum pulse results

Figures 8–17 illustrate the electromagnetic field results. These results were generated from computer codes that were constructed directly from Eqs. (3.4), (3.16), and (3.17). The codes were run under double precision on a Digital Equipment Corporation VAX11/785 computer hosting the DISSPLA graphics library. The results show that the tweaked MPS pulses have the desired propagation characteristics. All field quantities are normalized to their maximum value at $t=0$.

In Figs. 8–17 the MPS parameters are $a=1.0$ m, $\alpha=1.0$, $b=1.0\times10^{14}$ m^{-1}, $\beta=6.0\times10^{15}$, and $z_0=1.0\times10^{-2}$ m. Figures 8–12 show surface plots and the corresponding contour plots of the respective field quantities: the Hertz potential function f, the electric field component E_θ, the magnetic field component H_r, the Poynting flux component P_z, and the energy density U, relative to the pulse center locations $z=0.0$ km and $z=9.42\times10^2$ km. The transverse space coordinate ρ is measured in meters; the longitudinal space coordinate $z-ct$ is the distance in meters along the direction of propagation away from the pulse center $z=ct$. The real part of (3.4) was used to generate Fig. 8; the imaginary part of (3.4) was used in the generation of the field terms in Figs. 9–17. This choice was made strictly for convenience and does not detract from the generality of these results. It simply allows the amplitudes of all the quantities to be maximum at $z=t=0$. Notice that in contrast to the scalar field Re(f) which takes its maximum along the z axis at $\rho=0$, $z=ct$, the EM field components E_θ and H_r attain their maxima just slightly off the z axis at $\rho\neq0$, $z=ct$ and have nulls at $\rho=0$, $z=ct$. This is due to the derivatives ∂_r in (3.10) for those components.

The spatial window in Figs. 11 and 12 is smaller than in Figs. 8–10 to allow adequate visualization of the local variations of P_z and U away from the center of the pulse. The smallness of the field components in Figs. 9 and 10 in the off axis or "tail" regions results in even smaller product quantities such as $P_z=-E_\theta H_r$ and the energy density $U=\epsilon|\mathbf{E}|^2+\mu|\mathbf{H}|^2$ in those regions. This recommends at least the zooming employed here. A vector plot of the power flow (Poynting's flux) at 942 km is also identical to the corresponding plot at $z=0.0$ m. The power flow is highly directive in the desired direction since the longitudinal magnetic field component H_z is relatively small in comparison to the other field components for this choice of the MPS parameters.

Figure 13 represents a cross section along $z-ct$ of Fig.

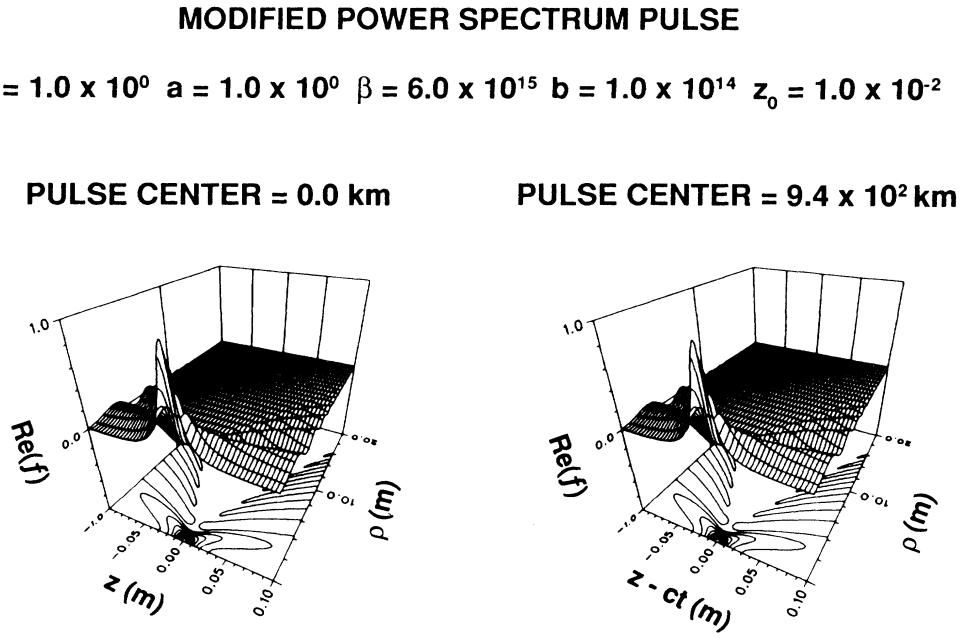

FIG. 8. The modified-power-spectrum pulse is localized along the direction of propagation and recovers its initial amplitude at large distances. The real part of the MPS pulse is shown for the parameters $a=1.0$ m, $\alpha=1.0$, $b=1.0\times10^{14}$ m^{-1}, $\beta=6.0\times10^{15}$, and $z_0=0.01$ m.

9 where E_θ is a maximum; in particular, it is the time history of the field component E_θ measured at $\rho=0.40$ m, $z=942$ km. This time history is identical to the one measured at $\rho=0.40$ m, $z=0.0$ m and at every $\rho=0.40$ m, $z=n\pi$ m, n a positive integer, until $z\sim3.0\times10^{15}$ m. The Fourier transform of this function is given in Fig. 14. This spectrum has its maximum at 8.40 GHz. The tail regions are not higher-frequency oscillations. They ap-

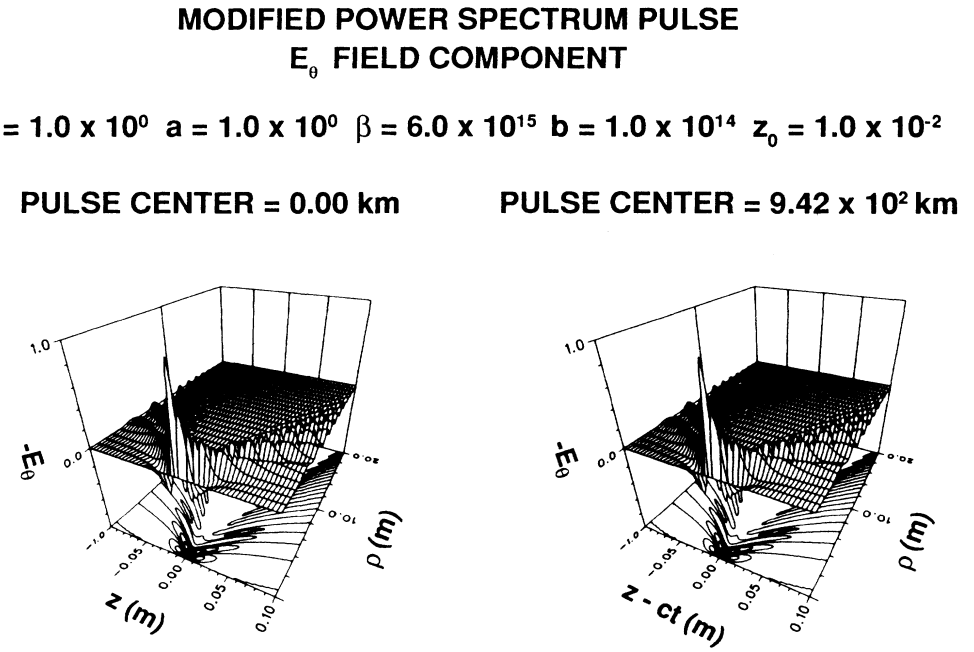

FIG. 9. The electric field component E_θ of the electromagnetic MPS pulse is shown for the parameters $a=1.0$ m, $\alpha=1.0$, $b=1.0\times10^{14}$ m^{-1}, $\beta=6.0\times10^{15}$, and $z_0=0.01$ m.

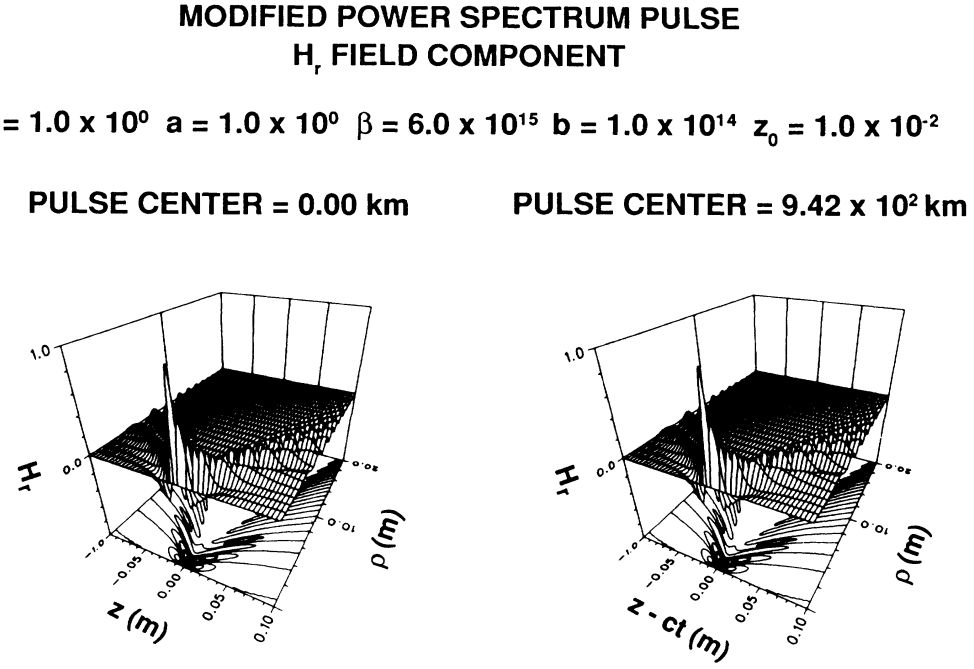

FIG. 10. The magnetic field component H_r of the electromagnetic MPS pulse is shown for the parameters $a=1.0$ m, $\alpha=1.0$, $b=1.0\times10^{14}$ m^{-1}, $\beta=6.0\times10^{15}$, and $z_0=0.01$ m.

pear in the field quantity plots but not the scalar function one because their amplitudes are negligible in the latter case. The derivatives in (3.10) accentuate their presence in the electromagnetic field quantities. The time histories measured at a point (ρ,z) have more oscillations further away from $z=ct$ as ρ increases; their spectra fill in the spectrum of the field time history at its maximum, Fig. 14.

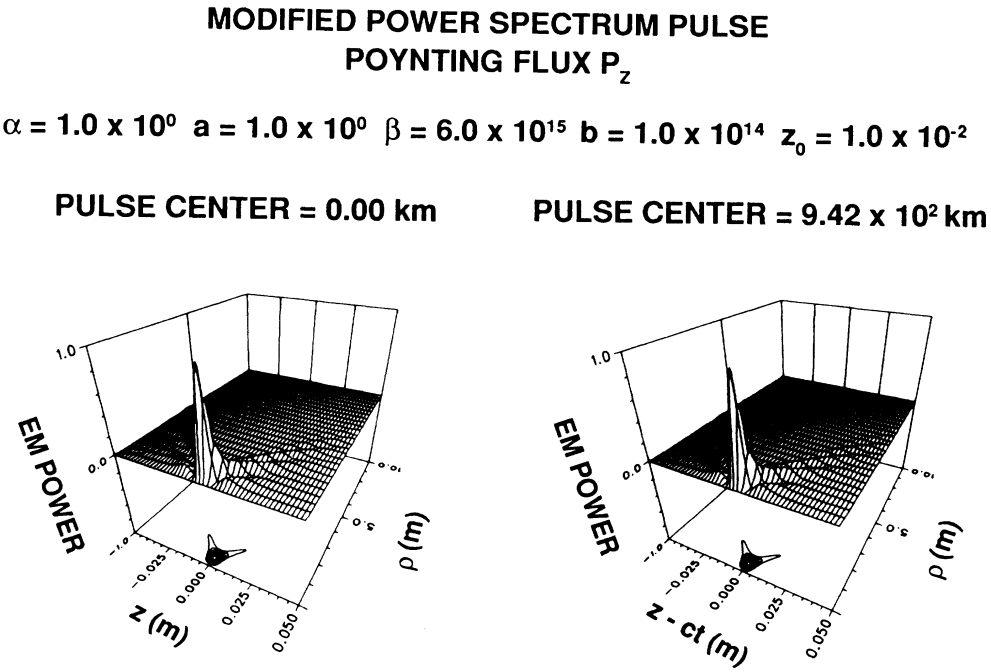

FIG. 11. The corresponding Poynting flux component P_z of the electromagnetic MPS pulse is shown for the parameters $a=1.0$ m, $\alpha=1.0$, $b=1.0\times10^{14}$ m^{-1}, $\beta=6.0\times10^{15}$, and $z_0=0.01$ m.

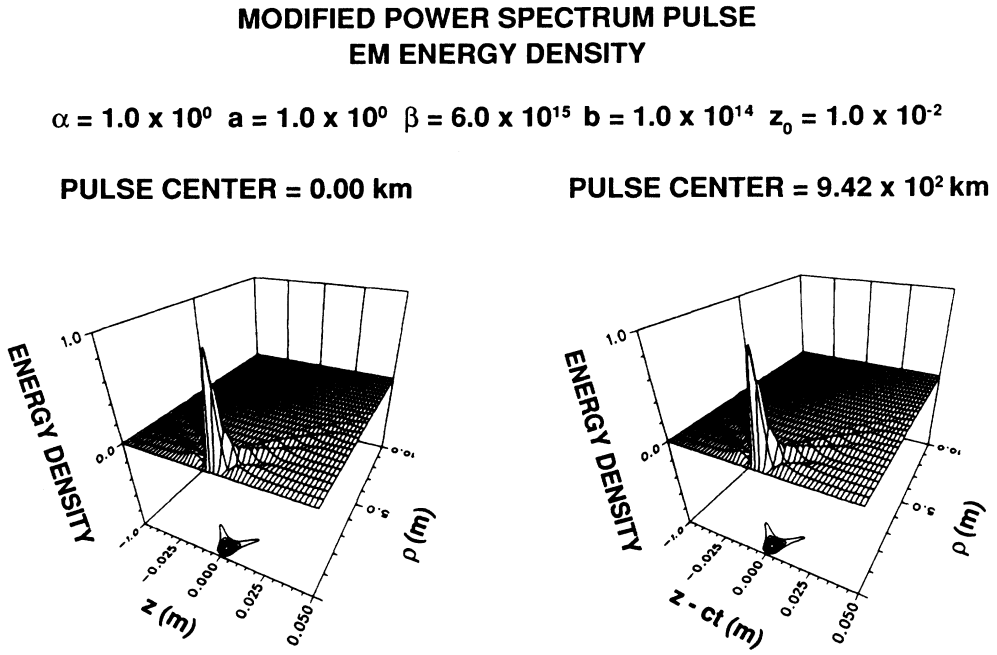

FIG. 12. The corresponding electromagnetic-field-energy density U of the electromagnetic MPS pulse is shown for the parameters $a=1.0$ m, $\alpha=1.0$, $b=1.0\times10^{14}$ m^{-1}, $\beta=6.0\times10^{15}$, and $z_0=0.01$ m.

The behavior of the MPS pulse at a time where this field does not attain its maximum is illustrated in Fig. 15. Surface plots and the corresponding contour plots of the MPS pulse energy density U are given relative to the pulse center locations $z=0.0$ km and $z=1.50\times10^3$ km. As noted above, the plots show that the field is shifted to locations about the pulse center.

In Figs. 16 and 17 the pulse-center distance of the second plot of Fig. 9 of the electric field component E_θ and of Fig. 12 of the EM energy density U has been increased to $z=9.42\times10^9$ km. The pulse-center distance has been greatly increased in these figures to illustrate the invariance of the field shape over much larger distances.

These results definitively show the localization of the field near the direction of propagation over very large distances. In fact, the electromagnetic MPS pulse is dramatically better than the corresponding diffraction-limited Hermite-Gaussian laser field. Let the waist of a zeroth-order laser field at $z=0$ be w_0 and let λ be its wavelength. Along the direction of propagation its amplitude varies at $1/[1+(\lambda z/\pi w_0^2)^2]^{1/2}$, so that the far-

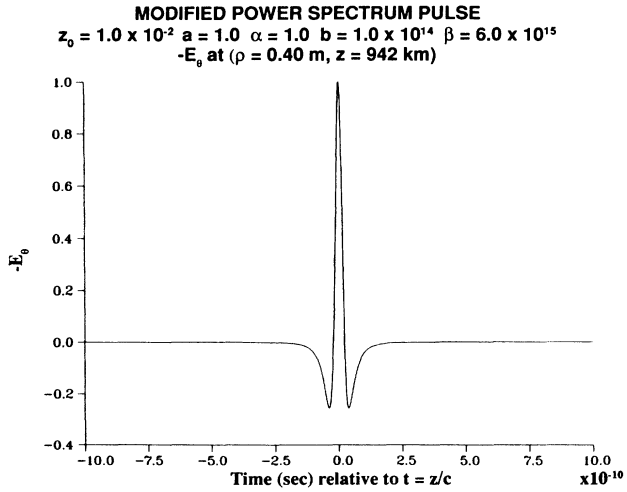

FIG. 13. The time history of the field component E_θ shown in Fig. 9 is given at the point $\rho=0.40$ m, $z=942$ km where it achieves its maximum.

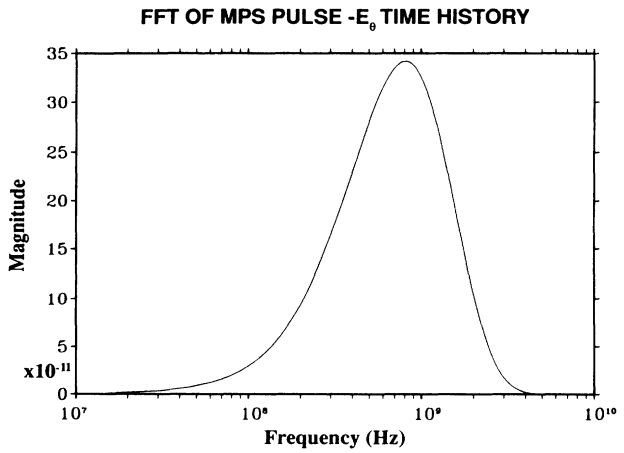

FIG. 14. The Fourier transform of the time history in Fig. 13 shows that the pulse spectrum is localized about 8.4 GHz.

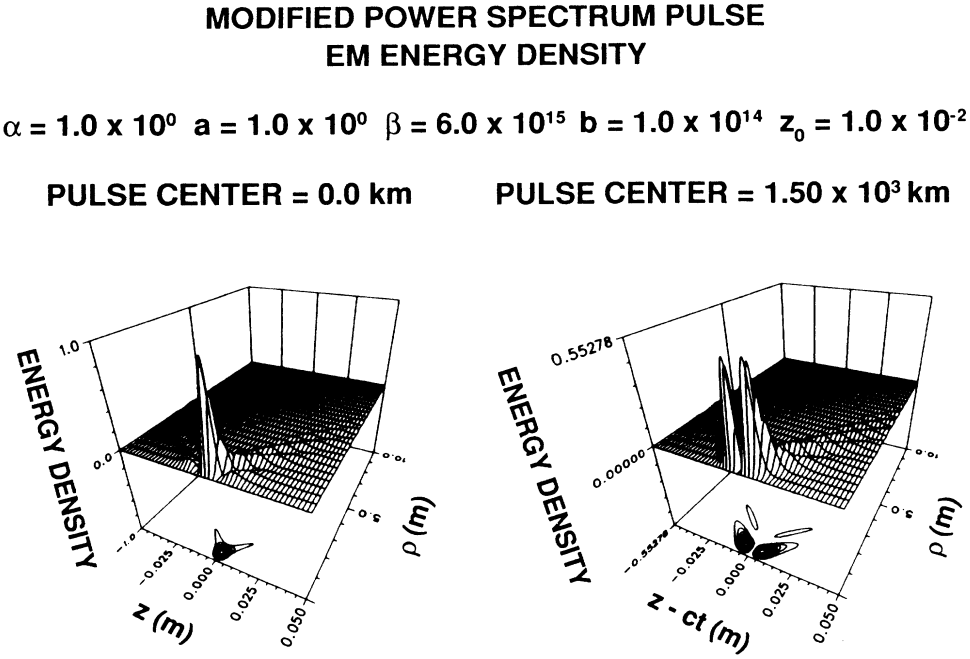

FIG. 15. The electromagnetic field energy density U of the MPS pulse is shown at a distance where it is not a maximum at $z=ct$. The energy density remains localized near the direction of propagation but has reorganized itself around the plane $z=ct$.

field boundary, where it begins to decay as $1/z$, is nominally reached when $z\sim\pi w_0^2/\lambda$. The square of the amplitude at that point is 0.50 times its initial value. The angular spread of this laser field is $\theta\sim\lambda/\pi w_0$ in the far field. Now with the above MPS pulse parameters $w_0=(b/\beta z_0)^{-1/2}=1.3$ m. The highest frequency of the spectrum shown in Fig. 14 is found by integrating its square, the power spectrum. There are no spectral components above 50.0 GHz$=5.0\times10^{10}$ Hz. The corresponding wavelength is $\lambda_{\min}=0.006$ m. For the equivalent diffraction-limited laser field these defining parameters give the distance to the far field:

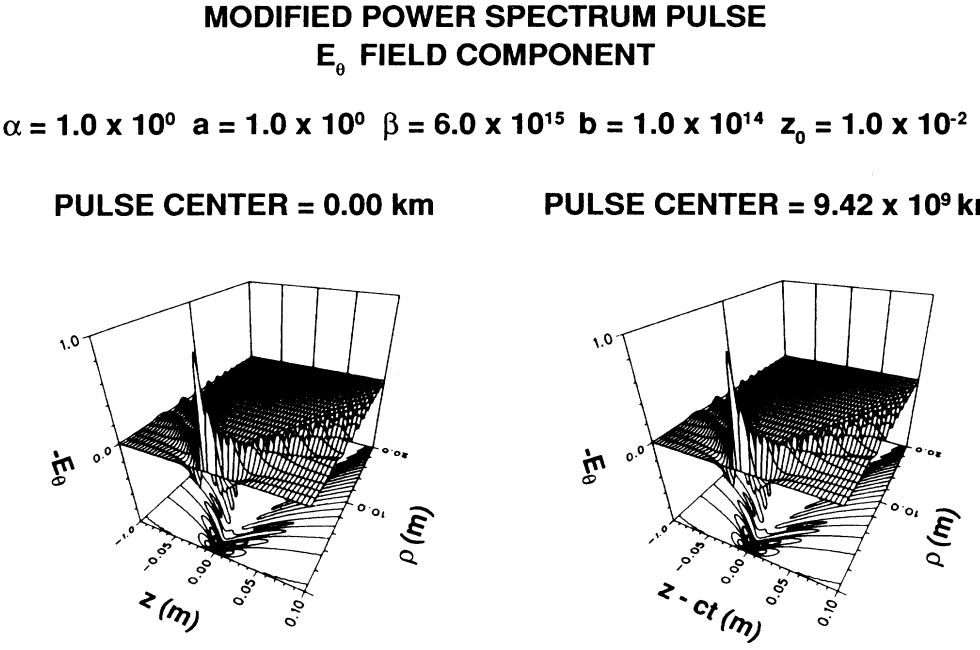

FIG. 16. The electric field component E_θ of the electromagnetic MPS pulse remains localized even at extremely large distances; $a=1.0$ m, $\alpha=1.0$, $b=1.0\times10^{14}$ m^{-1}, $\beta=6.0\times10^{15}$, and $z_0=0.01$ m.

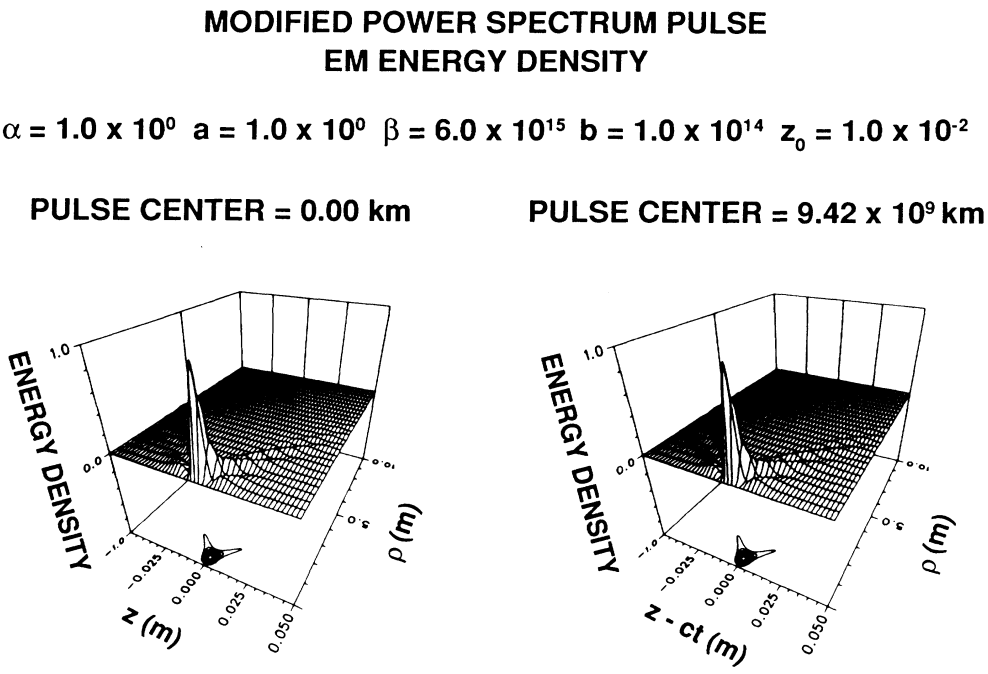

FIG. 17. The field energy density U of the electromagnetic MPS pulse remains localized even at extremely large distances; $a=1.0$ m, $\alpha=1.0$, $b=1.0\times10^{14}$ m^{-1}, $\beta=6.0\times10^{15}$, and $z_0=0.01$ m.

$$\frac{\pi w_0^2}{\lambda}\sim 0.872 \text{ km},$$

and the spread of the field at 10^{10} km,

$$\left[\frac{\lambda}{\pi w_0}\sim 1.5\times10^{-3}\right]\times10^{10} \text{ km}\sim 1.5\times10^{7} \text{ km}.$$

The field amplitude at 10^{10} km is essentially 10^{-10} its initial value. The localization of the electromagnetic MPS pulse near the z axis and the recovery of its initial amplitude well beyond the classical far-field distance confirms that the MPS pulse has propagation characteristics which are much better than the corresponding diffraction-limited Hermite-Gaussian laser field. The immediate question of practical realization of this result is addressed in Sec. IV.

Note that the parameters a, α, b, β, and z_0 of the MPS pulse were selected here to achieve a pulse with a microwave spectrum. They can be varied to design pulses with different characteristics. The effect of decreasing z_0 is to decrease the localization of the pulse near the z axis, as is readily seen from Eq. (3.6), and to increase the center frequency of the pulse. A factor of 10 decrease in z_0 results approximately in a factor of 10 increase in the center frequency. A slight decrease in the number of oscillations in the "tail" regions is also realized as z_0 is decreased. The effect of increasing b is to increase the localization of the pulse near the z axis, as is readily seen from Eq. (3.6). This occurs with a penalty of an increase in the number of oscillations everywhere.

IV. PHYSICAL REALIZATION

The results of Secs. II and III have demonstrated the existence of solutions of the homogeneous medium, source-free wave and Maxwell's equations that have the physical properties of localized propagation and amplitude maintenance over very large distances. They also demonstrated that the "tweaked" MPS pulses are not physically pathological. Consequently, we have in hand interesting theoretical pulses. Moreover, these solution are extremely appealing for a number of potential applications. Next, it must be determined if fields such as these MPS pulses can be replicated by a finite set of sources, e.g., by a finite planar array of radiating elements. The hope is to produce fields that would be extremely close facsimiles of the exact solutions. As will be shown below, the MPS pulse can be recovered to a high degree of accuracy from a finite planar array of sources. The array-generated MPS pulse appears to be very robust and insensitive to perturbations in the initial aperture distributions. What is unusual about this array is the fact that the aperture distribution is modulated spatially and temporally, while the individual time histories have a large bandwidth.

A. Huygens's reconstruction

The physical realization of the scalar MPS pulse was simulated by launching it from a finite planar array of point sources with the causal, time-retarded Greens function. The essential idea is that with an array of point sources one is always in the far field of each radiator, and the overall field response of the array is readily obtained by superposition. In this simulation, each element of the

array is driven with a (potentially different) time function specified by the exact field.

Any scalar field $V(\mathbf{r},t)$ can be defined within any closed surface S through the Green's function or Huygens's representation:[43]

$$V(\mathbf{r},t)=\int_S \{g(\mathbf{r},\mathbf{r}')(\partial_{n'}V)(\mathbf{r}',t-R/c) - V(\mathbf{r}',t-R/c)[\partial_{n'}g(\mathbf{r},\mathbf{r}')] + g(\mathbf{r},\mathbf{r}')(\partial_{ct}V)(\mathbf{r}',t-R/c)\partial_{n'}R\}dS' , \tag{4.1}$$

where n' is the inward pointing normal to S, where the distance between the source coordinates $\mathbf{r}(x',y',z')$ on S and the observation coordinates $\mathbf{r}=(x,y,z)$ in the volume contained by S is

$$R=[(x-x')^2+(y-y')^2+(z-z')^2]^{1/2}$$

and the propagator

$$g(\mathbf{r},\mathbf{r}')=\frac{1}{4\pi|\mathbf{r}-\mathbf{r}'|} . \tag{4.2}$$

The reconstruction of the MPS pulse is accomplished with a discrete version of the Huygens representation of the field to the right of an infinite plane $z'=$const:

$$f(\mathbf{r},t)=-\int_{-\infty}^{\infty}dx'\int_{-\infty}^{\infty}dy'\,\Psi(x',y',z',t-R/c)\frac{1}{4\pi R} . \tag{4.3}$$

The z-plane constant is determined by the requirement that the field and its derivatives be zero on this plane at $t=0$.

The driving functions for the array elements were determined by the exact solution. In particular, they are

$$\Psi(x',y',z',t-R/c) =[\partial_{z'}f]-[\partial_{ct'}f]\frac{(z-z')}{R}-[f]\frac{(z-z')}{R^2} . \tag{4.4}$$

For the MPS pulse one has explicitly

$$\partial_z f=\left[-\frac{1}{\beta}\left[b+\frac{\alpha}{s/\beta+a}\right]\partial_z s-\frac{i}{z_0+i\tau}\right]f , \tag{4.5a}$$

$$\partial_{ct} f=\left[-\frac{1}{\beta}\left[b+\frac{\alpha}{s/\beta+a}\right]\partial_{ct} s+\frac{i}{z_0+i\tau}\right]f , \tag{4.5b}$$

where the requisite derivative terms of s are given after Eqs. (3.17). The aperture was made finite by truncating the limits in (4.3) to some specified size. As will be shown in Sec. IV B, computer simulations have demonstrated that the MPS pulse can be recovered to a close approximation from a finite array at very large distances from it.

The electric field can also be defined within any closed surface S through the Huygens representation analogous to (3.1). The latter employs only the electric field and its derivatives on S.[10,43] An alternate (but related) representation employing only the tangential electric and magnetic field and their derivatives on S is also possible.[10,43] Reconstruction of the MPS electromagnetic pulse field components from a finite array is currently under investigation. Only scalar field results will be presented below.

B. Finite-array results

The Huygens representation (4.3) of the MPS pulse (3.4) has been implemented numerically in a variety of configurations. These include circular, rectangular, and hexagonal arrays of equally spaced elements. For instance, for a rectangular array with $(N+1)\times(M+1)$ equally spaced elements, (4.3) is approximated as

$$f(\mathbf{r},t)=-\sum_{n=-N}^{+N}\sum_{m=-M}^{+M}[\Psi(n\,\Delta x,m\,\Delta y,z',t-R_{nm}/c)\Delta x\,\Delta y]\frac{1}{4\pi R_{nm}} , \tag{4.6}$$

where the spacings are Δx in x and Δy in y and the distances $R_{nm}=[(x-n\,\Delta x)^2+(y-m\,\Delta y)^2+(z-z')^2]^{1/2}$. On the other hand, when the observation point lies along the z axis, the axisymmetric nature of the MPS pulse reduces (4.3) to 2π times a radial integral. In this case it is most cost effective to calculate (4.3) from a finite circular array with distinct, equally spaced annular sections:

$$f(\rho=0,z,t)=-\sum_{n=0}^{+N}[\Psi(\rho_n',z',t-R_n/c)\mathcal{A}(n)]\frac{1}{4\pi R_n} , \tag{4.7}$$

where the distances $\rho_n'=n\,\Delta\rho'$ and $R_n=[(\rho_n')^2+(z-z')^2]^{1/2}$ and the area weighting of the annulus labeled by n is $\mathcal{A}(n)=\pi[(\rho_n'+\Delta\rho'/2)^2-(\rho_n'-\Delta\rho'/2)^2]^{1/2}=2\pi\rho_n'\,\Delta\rho'$. The annular regions are assumed to represent a fixed number of radiating elements in the azimuthal direction. This will be the form utilized below. Nonuniformly spaced arrays and adaptive beam-forming techniques have not yet been employed. The following results simply represent a straightforward, brute-force approach to determine the possibility of launching a MPS pulse facsimile.

The question raised in Ref. 29 about the causal properties of the FWM prompted an investigation of the full Green's-function representation for the MPS pulse. In particular, the representation

$$f(\mathbf{r},t)=f^+(\mathbf{r},t)+f^-(\mathbf{r},t) \tag{4.8}$$

was utilized for the purpose of characterizing the amount of advanced Green's-function contribution required for this reconstruction process. The forward- and the backward-propagating Green's-function components are, respectively,

$$f^+(\mathbf{r},t)=-\int_{-\infty}^{\infty}dx'\int_{-\infty}^{\infty}dy'\,\Psi(x',y',z',t-R/c)\frac{1}{4\pi R} , \tag{4.8a}$$

$$f^-(\mathbf{r},t)=-\int_{-\infty}^{\infty}dx'\int_{-\infty}^{\infty}dy'\,\Psi(x',y',z',t+R/c)\frac{1}{4\pi R} . \tag{4.8b}$$

It was found numerically that

$$f^{-}(\mathbf{r},t) \leq 10^{-20} f^{+}(\mathbf{r},t) \tag{4.9}$$

for any of the cases considered. This means that the MPS pulse is reconstructed *only* from the causal, forward-propagating components in the Huygens representation of the field.

Consider again the MPS pulse featured in Figs. 5–7, which has the parameters $a=1.0$ cm, $\alpha=1.0$, $b=1.0\times10^{10}$ cm^{-1}, $\beta=6.0\times10^{15}$, and $z_0=1.667\times10^{-3}$ cm. The time history of the field (solid line) reconstructed at the observation point $\rho=0.0$ m, $z=1.0$ km along the z axis from a circular array of radius $r_{\max}=0.5$ m is compared to the time history of the exact field (dashed line) in Fig. 18. The array is assumed to have 101 element sections and to be located in the plane $z'=0.001$ m. The observation distance and the array's radius are increased, respectively, to $z=10.0$ km and $r_{\max}=5.0$ m in Fig. 19. There are 1001 time points in each of these figures. The time axis represents the time relative to the pulse center time $t=z/c$. Large negative times thus represent times before the arrival of the pulse. Aside from the late-time noise, the pulse reconstructions are remarkably good. Similar results are also obtained when the observation point is off-axis.[10] Generally, if the pulse is reconstructed well on-axis, it will also be reconstructed well off-axis.

A quantitative measure of the size of a circular array needed to reconstruct the MPS pulse at increasingly larger axial distances is shown in Fig. 20. The field values at the axial distances $z=1.0$, 10.0, 100.0, 1000.0, and 10 000.0 km generated by a finite circular array are plotted against the radius of that array. The curves become horizontal when the exact field value is reached. Clearly, the size of the array controls the reconstruction distance. The scaling ratio is approximately a factor of 10 increase in radius size in centimeters for a factor of 10 increase in distance along the direction of propagation in kilometers. A smaller array, however, does not increase the transverse width of the pulse, but only degrades the reconstruction. As the array size is increased, the pulse definition is enhanced relative to the surrounding fields.

One outstanding question is: "Where is the Fresnel zone–far-field boundary or Rayleigh distance, $\pi w_0^2/\lambda$?" Unfortunately, the question does not have a definitive answer here because of the pulsed nature of these solutions. Those concepts are closely tied to cw excitations, antennas, and wave propagation. Nonetheless, as a matter of comparison, the Rayleigh distance has been

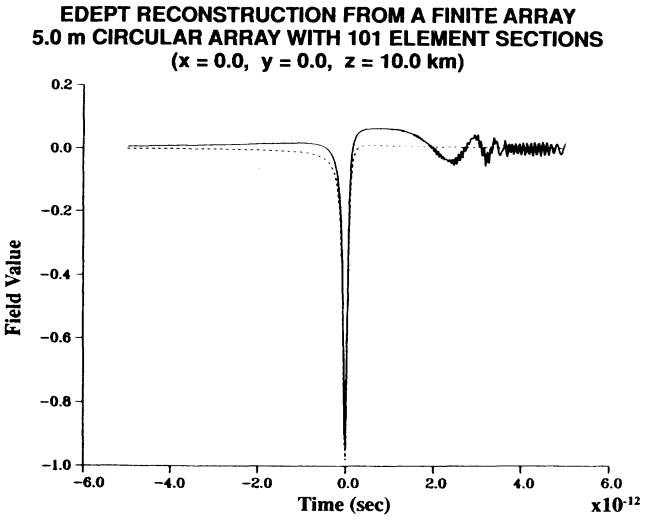

FIG. 19. The same MPS pulse is now compared to the reconstructed pulse (——) generated by a 5.0-cm circular array with 101 element sections at the point $\rho=0.0$ m, $z=10.0$ km.

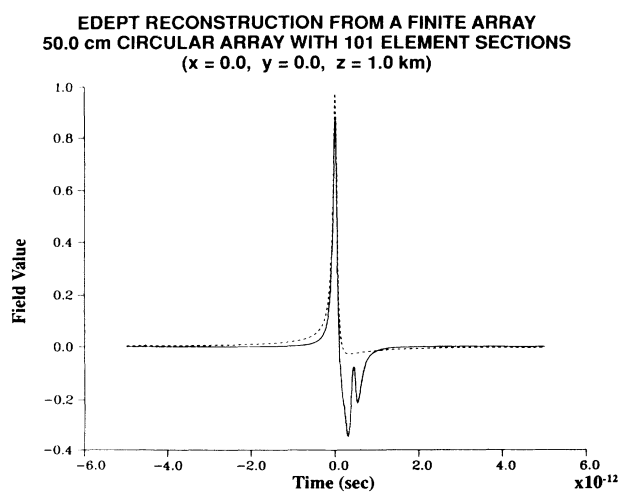

FIG. 18. The exact MPS pulse (— — —) with the parameters $a=1.0$ cm, $\alpha=1.0$, $b=1.0\times10^{10}$ cm^{-1}, $\beta=6.0\times10^{15}$, and $z_0=1.667\times10^{-3}$ cm is compared to the reconstructed pulse (——) generated by a 50.0-cm circular array with 101 element sections at the point $\rho=0.0$ m, $z=1.0$ km.

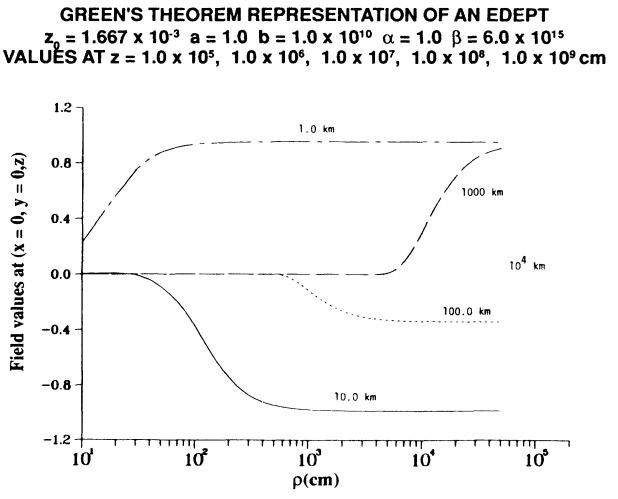

FIG. 20. As the observation point is moved further away from the sources, the size of the array needed to generate the MPS pulse increases. The values of the reconstructed pulse at $z=1.0$, 10.0, 100.0, 1000.0, and 10 000.0 km generated by a circular array are plotted against the radius of the array to illustrate this effect.

used by others as a figure of merit for comparisons with the array-launched MPS pulse.

Referring to Fig. 7, one finds the spectrum of the MPS pulse under consideration deviates from a constant level around 30.0 GHz, begins to steeply roll off to zero around 200.0 GHz, but still has nontrivial components approximately out to 1.5×10^{13} Hz. The first frequency corresponds to the wavelength $\lambda=1.0$ cm, the second to $\lambda=1.5\times10^{-1}$ cm, and the last to $\lambda=2.0\times10^{-3}$ cm. At 1.0 km the first wavelength gives a critical circular array radius $r_c\sim[(1.0\text{ cm})(1.0\times10^5\text{ cm})/\pi]^{1/2}=178.4$ cm, the second gives $r_c\sim[(1.5\times10^{-1}\text{ cm})(1.0\times10^5\text{ cm})/\pi]^{1/2}=69.1$ cm, and the last gives $r_c\sim[(2.0\times10^{-3}\text{ cm})(1.0\times10^5\text{ cm})/\pi]^{1/2}=8.0$ cm. The 50.0-cm array radius in Fig. 18 is smaller, about equal to, and much larger than these values. Thus, for a majority of the spectral content of this MPS pulse, the Fresnel–far-field boundary can be reached from a finite array. Whether it is or is not completely reached may be a moot point and depends on the intended application. These results alone indicate that from a modest size array, energy can be transmitted locally without spreading over sufficiently large distances to be of significant interest.

In both Figs. 18 and 19, one finds the front part of the pulse reproduced exceptionally well. The element spacing has a strong effect on the behavior of the back of the pulse. This is most notable in Fig. 19. Taking the middle value $\lambda=0.15$ cm, the source spacing is $\sim3\lambda$ for the 50-cm array and $\sim30\lambda$ for the 500-cm array. Increasing the source density, the number of source elements in the array, decreases this late-time oscillation. The array size also influences the smoothness of the pulse. A large array will produce smaller amplitude oscillations in the back of the pulse.

A planar array used as a potential MPS pulse launching system would be the simplest array to field as a proof-of-principle experiment. However, there has been concern about the sensitivity of these array results to perturbations in the initial driving-time histories and their effects on the reconstruction of the MPS pulse. We have checked many of these concerns and were surprised at the results.

In the first perturbation analysis we applied an amplitude taper to the aperture driving functions. The principal taper we investigated was a Hanning window. We found that the amplitude taper actually helped the pulse reconstruction by decreasing the late-time oscillations and the source density. This occurred with a penalty in the peak amplitude. With a slightly larger aperture size and the amplitude taper, a very much improved recon-

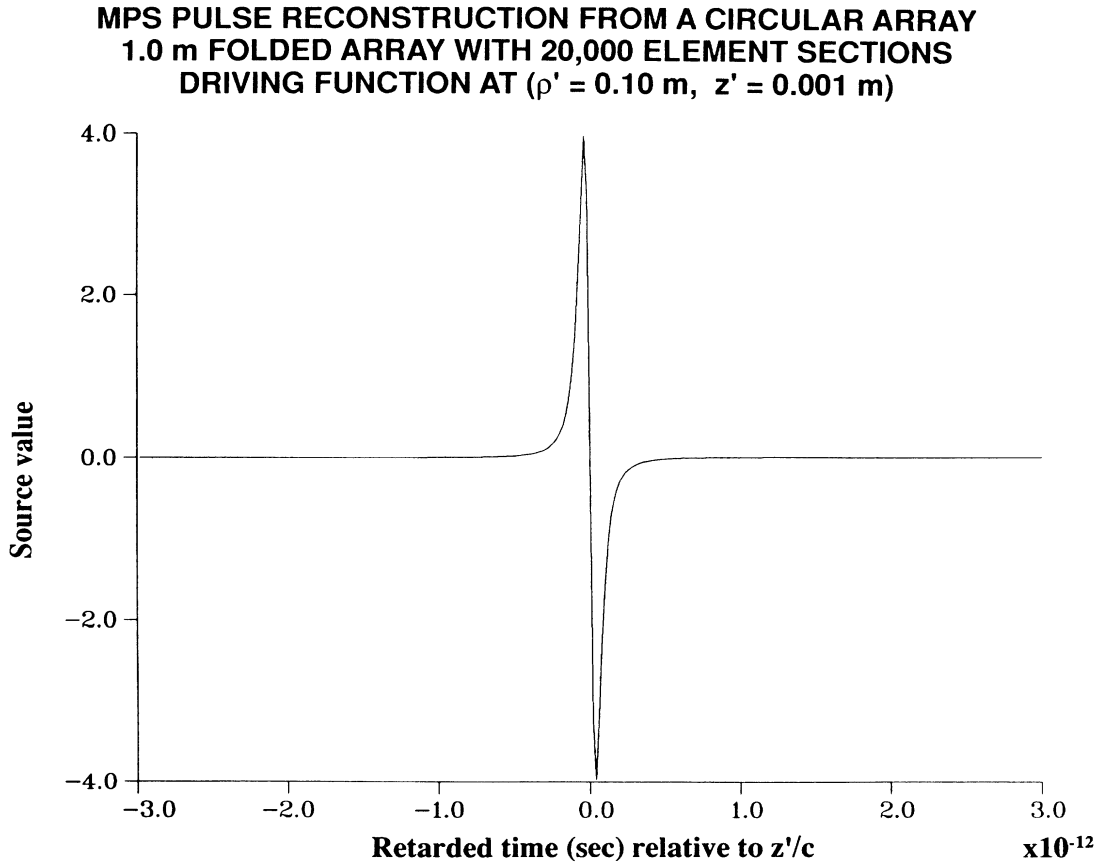

FIG. 21. The time history of the area-weighted driving function applied to the source at $\rho'=0.1$ m, $z'=0.001$ m in a 20000-element section, 1.0-m circular array is shown.

struction of the MPS pulse was actually achieved. The effect of the taper is to remove all of the low-frequency components of the field and to slightly emphasize the high-frequency ones.

Next, the effect of actually frequency filtering the driving functions was considered. The late-time oscillations occur because of the presence of undesirable, ill-behaved higher-frequency components which become emphasized in the superposition. Despite the presence of these components, the essential features of the MPS pulse are reproduced. To gauge the effect of removing some of these unwanted components, a low-pass, second-order Butterworth filter whose cutoff frequency is 250 GHz was applied to the initial driving functions. Much of the late-time noise was removed at a slight cost in the peak value; yet the essential features of the MPS pulse remained.

The stability of the MPS pulse reconstruction was further tested by applying random Gaussian noise to the individual driving functions. Despite the addition of substantial amounts of noise to the initial driving functions, the general features of the MPS pulse were recovered by the corrupted, array-generated pulse.

All of these results are very tantalizing and suggest that the array-reconstructed MPS pulse is not very sensitive to perturbations in the initial driving functions. These array signal processing and pulse-reconstruction stability issues are still being pursued.

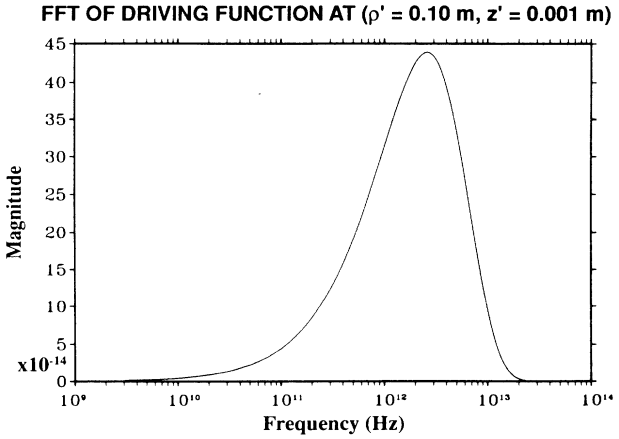

FIG. 22. The Fourier transform of the driving function in Fig. 21 shows a spectrum of frequencies centered near 3000 GHz with most of its energy being below 1.0×10^{13} Hz.

The difficulty of defining the Fresnel–far-field boundary is also compounded by the fact that the excitation does not have a spectrum identical to the desired field, but to its derivative. Figures 21–24 show the area-weighted driving function in (4.7) of $\rho'=10.0$ and 50.0 cm and their respective Fourier transforms for a 1.0-m radius circular array with 20 000 element sections. Because the dominant terms of the driving functions involve

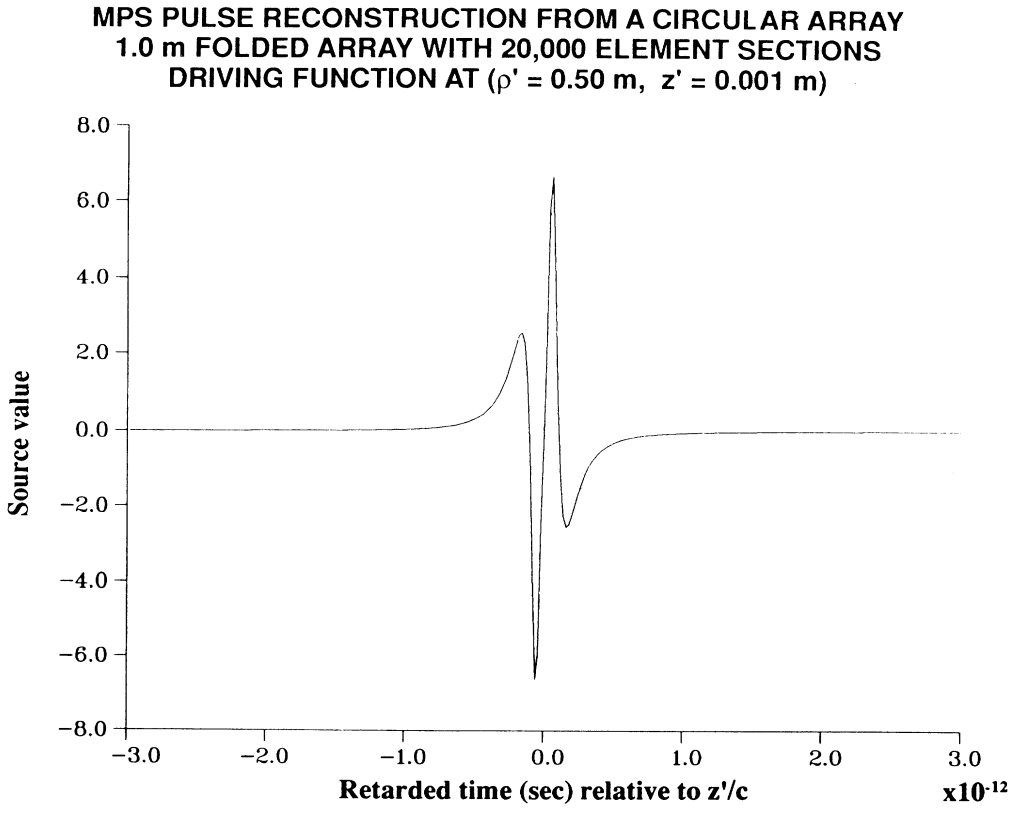

FIG. 23. The time history of the area-weighted driving function applied to the source at $\rho'=0.50$ m, $z'=0.001$ m in a 20 000-element section, 1.0-m circular array is shown.

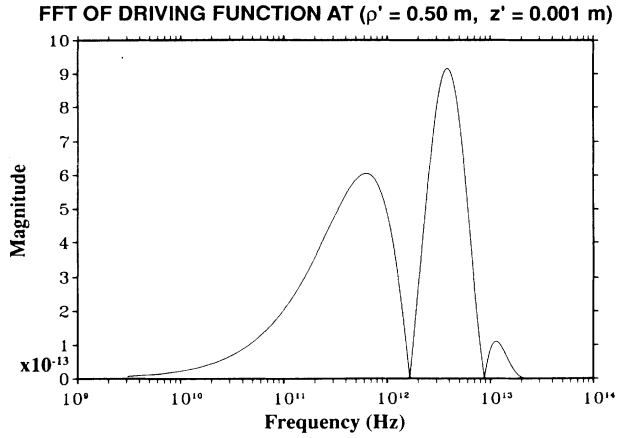

FIG. 24. The Fourier transform of the driving function in Fig. 23 shows a more complicated spectrum of frequencies, again with most of its energy being below 1.0×10^{13} Hz.

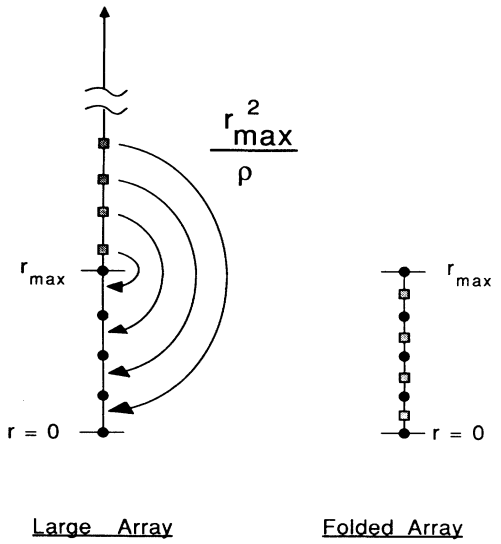

FIG. 25. An infinite array can be mapped conformally onto a finite array. This figure depicts this mapping and a resulting staggered array.

derivatives of the MPS pulse, one expects the absence of the dc components and the skew toward the higher frequencies found in Figs. 22 and 24. Moreover, notice that the spectrum of the driving function further from the z axis (Fig. 24) fills in the spectrum of the driving function nearer to the z axis (Fig. 22). This is also expected from the above discussion on the frequency content in the tails of the MPS pulse. One finds that the portion of the array at larger distances from the axis of symmetry is responsible for the larger wavelength components of the pulse. One also finds, however, that is responsible for recreating the pulse at larger distances from the array.

C. Folded-array results

Although they were not optimized, the simple circular arrays still reproduced the MPS pulse at significant distances from their location. However, it is still desirable to see how close to or how far beyond the classical Rayleigh length one can reach. Since a larger array reconstructs the desired pulse shape, what tricks, if any, are there to squeeze a larger array into a smaller one?

One suggestion is the folded array depicted in Fig. 25. The exterior of a planar circular array of radius $r_{\max}$ is "folded" onto its interior with the conformal map $\rho\rightarrow r_{\max}^2/\rho$. The folded array will be said to be staggered if, when the interior points are located at $n\,\Delta\rho$, the mapped exterior points are at $(n+\frac{1}{2})\Delta\rho$; unstaggered if the interior and mapped exterior points coincide. This folding trades a much less complicated source distribution for a more complicated one. In particular, Huygens's representation for a point on the z axis becomes

$$f(\rho=0,z,t)=-2\pi\int_0^{\infty}d\rho'\,\rho'\Psi(\rho',z',t-R/c)\frac{1}{4\pi R}$$
$$=-2\pi\int_0^{r_{\max}}d\rho'\,\rho'\Psi(\rho',z',t-R/c)\frac{1}{4\pi R}-\frac{2\pi}{r_{\max}^2}\int_0^{r_{\max}}d\xi\left[\frac{r_{\max}^2}{\xi}\right]^3\Psi(r_{\max}^2/\xi,z',t-R_e/c)\frac{1}{4\pi R_e}\,, \tag{4.10}$$

where $R_e=[(r_{\max}^2/\xi)^2+(z-z')^2]^{1/2}$. This is still an infinite-array representation. A finite one is obtained by approximating the distance $R_e\sim R$ in the denominator of the second integral and by introducing time offsets into the mapped source driving functions. In particular, set

$$f(\rho=0,z,t)\simeq-2\pi\int_0^{r_{\max}}d\rho'\,\rho'\Psi(\rho',z',t-R/c)\frac{1}{4\pi R}$$
$$-\frac{2\pi}{r_{\max}^2}\int_0^{r_{\max}}d\xi\left[\frac{r_{\max}^2}{\xi}\right]^3\Psi(r_{\max}^2/\xi,z',t-T(\xi,z';\rho=0,z)-R/c)\frac{1}{4\pi R}\,, \tag{4.11}$$

where now in the second term

$$R=[\xi^2+(z-z')^2]^{1/2} ,$$

$$T(\xi,z';\rho=0,z)=\{[(r_{\max}^2/\xi)^2+(z-z')^2]^{1/2}-[\xi^2+(z-z')^2]^{1/2}\}/c .$$

For the array this has the discrete form

$$f(\rho=0,z,t)\simeq -\sum_{n=0}^{+N}[\Psi(\rho_n',z',t-R_n/c)\mathcal{A}(n)]\frac{1}{4\pi R_n} - \sum_{m=0}^{+M}[\Psi(\xi_m,z',t-T(\xi_m,z',0,z)-R_m)/c)\mathcal{A}_e(m)]\frac{1}{4\pi R_m} , \tag{4.11'}$$

where the area weighting

$$\mathcal{A}_e(m)=\pi\{[r_{\max}^2/(\xi_m-\Delta\xi/2)]^2-[r_{\max}^2/(\xi_m+\Delta\xi/2)]^2\}=\frac{2\pi r_{\max}^4\Delta\xi}{\xi_m^3} .$$

The expression (4.11') allows one to treat the two contributions to the finite array separately. In the case of the staggered array, $\xi_m=(m+\frac{1}{2})\Delta\rho'$. On the other hand, for the unstaggered array, $\xi_m=m\,\Delta\rho'$, so that the reconstructed field (4.11') can be simply written as

$$f(\rho=0,z,t)\simeq\sum_{n=0}^{+N}\frac{S(\rho_n',z',t-R_n/c)}{4\pi R_n} , \tag{4.12}$$

which emphasizes the appearance of a more complicated set of sources.

Consider now a 1.0-m, folded circular array with 20 000 element sections. Let it be either stagered or not. In the staggered case both the interior and the mapped exterior portions of the array have 10 000 elements associated with each of them. The weighted driving function at the staggered point $\rho'=0.100\,05$ m of the array is shown in Fig. 26; its Fourier transform is given in Fig. 27. There are 1001 time points in Fig. 26. Figure 27 was constructed with a 16 384-point fast Fourier transform (FFT) of a 10 001-point time history extending from -0.1 to $+0.1$ ns. In contrast to the driving functions

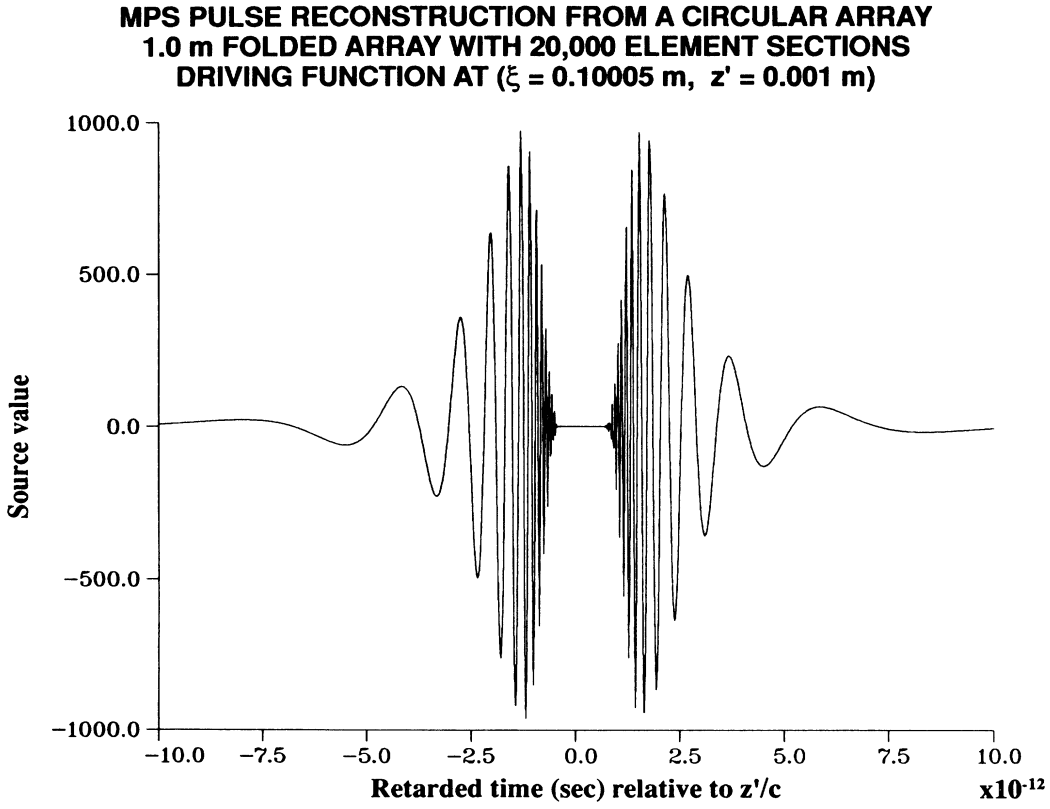

FIG. 26. The time history of the area-weighted driving function applied to the source at $\rho'=0.100\,05$ m, $z'=0.001$ m in a 20 000-element section, 1.0-m staggered circular array is shown.

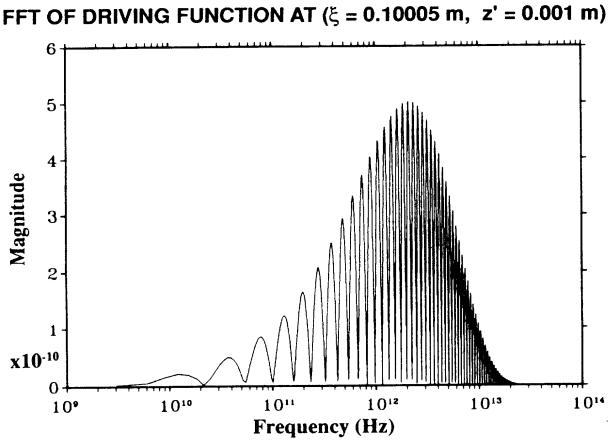

FIG. 27. The Fourier transform of the driving function in Fig. 26 shows a much more complicated spectrum of frequencies with most of its energy still remaining below 1.0×10^{13} Hz.

shown in Figs. 21–24, the curve in Fig. 26 is a larger amplitude, much more complicated time series. However, its spectrum does not contain any higher frequencies, only more resonances at the available ones.

The exact values of the MPS pulse along the direction of propagation are plotted in Fig. 28. They clearly confirm the analysis (3.5). Figure 29 gives the ratio of the reconstructed-to-the-exact-field value along the direction of propagation for the 20 000-element section unstaggered (solid line) and staggered (dashed line) 1.0-m arrays. There are 100 points per decade in these curves. With $f_{max}=1.5\times10^{13}$ Hz or $\lambda_{min}=2.0\times10^{-5}$ m and $w_0=0.316$ m, the Rayleigh limit is only $\pi w_0^2/\lambda_{min}=1.6\times10^4$ m. The larger bound $2D^2/\lambda_{min}=4.0\times10^5$ m. Thus one finds that this folded array produces a field which has surpassed the classical diffraction limit at least a thousandfold. The agreement between the reconstructed and exact field values is remarkable, especially consid-

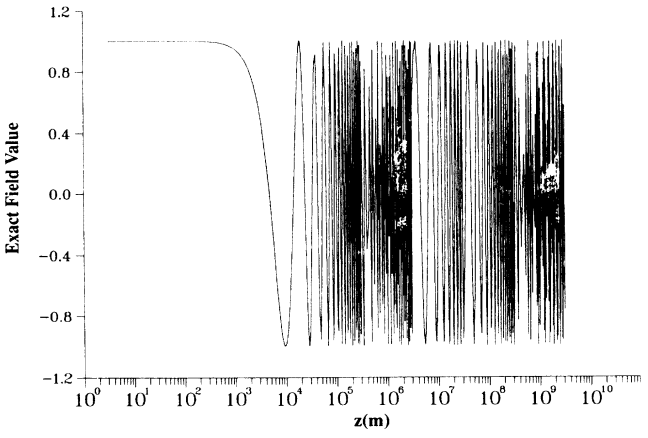

FIG. 28. The exact field value of the MPS pulse on axis is plotted against the distance along the direction of propagation.

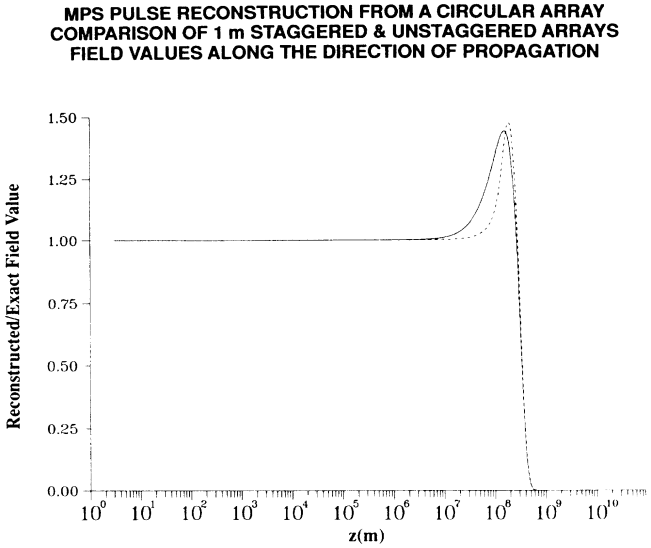

FIG. 29. The ratio of the reconstructed to the exact field value is plotted as a function of the distance from the array. The reconstructed MPS pulse is generated by 1.0 m folded, unstaggered (——) and staggered (— — —) circular arrays with 20 000-element sections. The Fresnel zone–far-field boundary is located at $z\sim3.0\times10^5$ m.

ering the sensitivity of their ratio when the exact values are very small. Note that these curves are very reminiscent of a Fresnel integral calculation. It may very well be that the MPS pulse reconstruction is simply pushing out the near field of this aperture to larger distances. However, it does so without broadening the pulse in the transverse direction.

The time history of the reconstructed pulse at $\rho=0.0$, $z=942$ km is compared to the exact MPS pulse in Fig. 30. It was generated by the 20 000-element staggered array. There are 1001 time points in both curves. Aside from the low-amplitude late-time oscillations, the agreement is very good.

It is found that the original, inner portion of the array is responsible for the pulse reconstruction up to approximately 10 km. The folded portion contributes very little to the field up to that point. After that point the roles are reversed; the folded portion of the array is responsible for recreating the pulse and the inner portion has little effect. This complementary action of the inner and folded portions of the array may be important for potential applications. One application may require good pulse reconstruction only near the aperture, while others may want a pulse to appear only at large distances. Moreover, from a practical point of view, keeping an inner and folded portion may pose a dynamic range problem for the amplitudes of the driving functions. The amplitudes of the area-weighted driving functions are much larger for the folded portion.

Because of the nature of the folding map, it is expected that a higher-density array will recreate the pulse at further distances, i.e., the folded portion of the array has elements very near the axis corresponding to very large

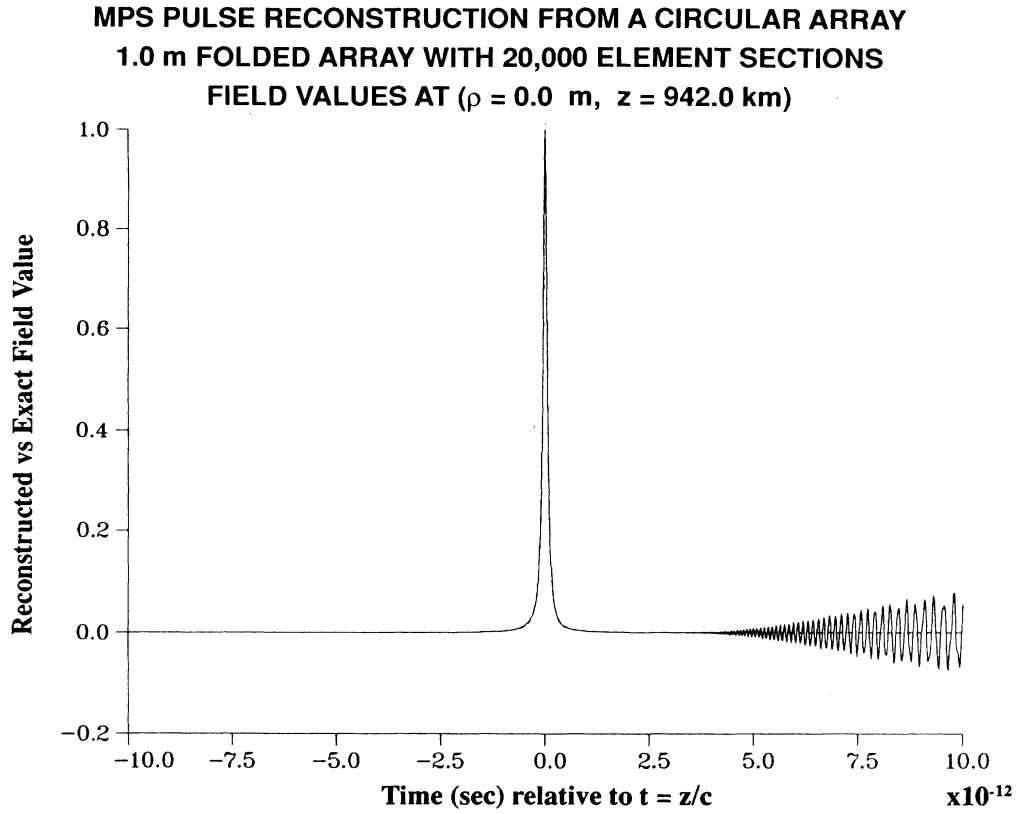

FIG. 30. The reconstructed pulse (——) at $\rho=0.0$ m, $z=942$ km generated by a 1.0-m, staggered, folded circular array with 20 000-element sections is compared to the exact MPS pulse (— — —).

transverse distances. For the 20 000-element section folded array, the element spacing is quite dense, there being approximately a 1.667λ spacing between the elements at the smallest wavelength. The effect of decreasing the number of element sections is shown in Fig. 31. The ratio of the reconstructed-to-the-exact-field value is plotted along the direction of propagation for distances exceeding the Rayleigh limit. The curves correspond to arrays having 200-, 2000-, and 20 000-element sections. Decreasing the number of sections by a factor of 10 decreases the distance beyond the Rayleigh length approximately by a factor of 10.

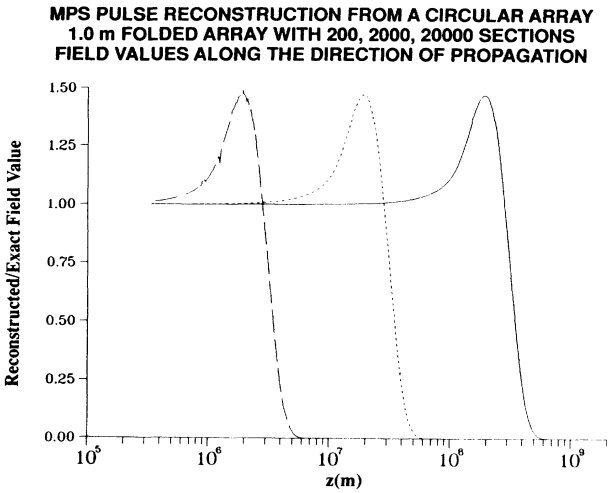

FIG. 31. The ratio of the reconstructed to the exact field value is plotted as a function of the distance from the array. The reconstructed MPS pulse is generated by 1.0-m folded, staggered circular arrays with 200 (—·—·—·), 2000 (— — —), and 20 000 (——)-element sections. The Fresnel zone–far-field boundary is located at $z\sim 3.0\times 10^5$ m.

V. DISCUSSION

This paper has shown that many interesting, exact pulse solutions of the wave and Maxwell's equations exist and that they provide local-energy transmission in space and time. One such pulse, the modified-power-spectrum pulse, was described in detail. It can be designed to recover its initial amplitude after propagating very large distances; moreover, the designed pulse can be confined to a region very near the direction of propagation. In particular, the MPS pulse has transmission characteristics superior to conventional Hermite-Gaussian laser fields. Having established the existence of this exact solution, described its properties, and demonstrated that it was not physically pathological, we addressed the question of practical realization.

It was shown that the MPS pulse can be recovered to a high degree of accuracy from a finite planar array of sources. In particular, a Huygens reconstruction based on a finite planar array of point sources reproduced the MPS pulses at large distances away from the array. This

array, in contrast to conventional cw-driven apertures, was driven by a spatial distribution of wide bandwidth time waveforms. The array-generated MPS pulse appears to be very robust and insensitive to perturbations in the initial aperture distributions. The latter include amplitude tapering the initial distribution, frequency filtering the initial time histories, and simply adding random noise to the initial driving-time histories. Even though the localization of the pulse was maintained near the direction of propagation, the simple array only seemed to flirt with the Rayleigh length and not definitively surpass it. One alternative array concept, the folded array, traded complexity in the source distribution for resoundly surpassing the Rayleigh distance.

These nonoptimized results are very tantalizing and suggest further investigations into the characteristics of these solutions and their potential launching mechanisms. One such effort would be a definitive, proof-of-principle experiment. An experiment has already been designed and fielded to study the acoustic version of these directed energy pulse trains, the ADEPT. A synthetic array was driven with a spatial distribution of time functions corresponding to the scalar MPS pulse. The results confirm the existence of this form of localized wave transmission for ultrasonic waves in water.[44] A number of practical issues such as array design and optimization and the propagation of ADEPT's through complex environments involving scattering and refraction are currently being studied.

Antennas and practical issues of realization aside, the solutions presented here are interesting in their own right. Exact solutions of any equation are extremely useful in understanding the basic physics that can be described by that equation. The solution procedure described here can be applied to other situations and equations of interest. For instance, these EDEPT pulses can be constructed in guiding structures such as waveguides.[45] It also leads to space-time generalizations of conventional Hermite-Gaussian laser modes.[46] The inversion procedure and its generalization (introduced in Refs. 2 and 42) have not been excercised much at all yet. They provide an alternative to Fourier (plane-wave) decompositions and can be exploited when transient, space-time phenomena are under investigation.

Another interesting example is a localized solution of the Klein-Gordon equation:

$$\left[\Delta-\partial_{ct}^2-\left[\frac{mc}{\hbar}\right]^2\right]\Phi=0\ , \tag{5.1}$$

which describes the behavior of a relativistic, spin zero, massive particle. It can be shown[47] that if the particle is moving with speed $v=pc^2/E$ along the z axis, then setting

$$\Phi(\rho,z,t)=e^{ik[z+(c^2/v)t]}F_k(\rho,z-vt) \tag{5.2}$$

and $p=\hbar k$, (5.1) reduces to the hyperbolized Schrödinger equation

$$\Delta_\perp F_k+4ik\partial_\tau F_k+\gamma^{-2}\partial_\tau^2 F_k=0\ , \tag{5.3}$$

where the relativistic term $\gamma=1/(1-v^2/c^2)^{1/2}$ and for this case the distance parameter $\tau=z-vt$. To leading order, if v is near c so that $\gamma\gg1$, then the second derivative term in τ is negligible and (5.3) becomes

$$4ik\partial_\tau F_k+\Delta_\perp F_k=0\ . \tag{5.4}$$

This is identical to Eq. (2.3). Proceeding as in Secs. II and III with the MPS pulse, one can then construct localized, finite-energy solutions of (5.1). Perturbation solutions of (5.3) can be extracted from work[46,48,49] describing Gaussian beams beyond the paraxial approximation.

What issues remain? First, aside from the creation of "photon torpedoes," there may be many potential applications for pulses which locally transmit wave energy. A number of obvious ones include microscopy, power transmission, secure communications, and remote sensing. There are probably many others and they should all be identified and simulated. Second, the MPS pulse is only one of an infinite number of new solutions that need to be investigated. It might be possible to design other EDEPT's, for instance, that have propagation characteristics similar to the MPS pulse but better launching properties. These pulses may also be tailorable to specified applications such as the above. Third, in contrast to conventional plane-wave analyses, these pulses or "macrophotons," are constructed from fundamental pulses that are themselves either plane-wave or clump like solutions of the wave and Maxwell's equations. This classical wave-particle duality is inherent in the superposition used to create the localized pulses. From a theoretical point of view this conclusion makes these solutions immensely interesting and its ramifications need to be clarified. Finally, from a practical point of view, the use of a planar array is probably the worst possible way to attempt the generation of an EDEPT such as the MPS pulse. The folded array was an attempt to optimize the propagation distance for a given array size at a cost of the simplicity of the source distribution. It still did not recover the MPS solution everywhere. The MPS pulse has a nontrivial, finite extent in space-time. Like conventional laser modes, which require a modal volume for their existence, the MPS pulses may require a finite-volume source of some sort for their "unrestricted" realization. A more optimal launch system design may be feasible and is under investigation.

ACKNOWLEDGMENTS

I would like to thank Mr. José Hernandez for his invaluable support on the signal-processing aspects of time-domain array-synthesized fields. I would also like to thank Mr. Ronald Schmucker for his assistance in making the computer software and hardware do what I needed it to do. I would also like to thank Professor I. Besieris, Mr. A. Shaarawi, Professor A. Gautesen, Professor L. Felsen, Professor E. Heyman, Dr. H. Zucker, and Dr. H. Brandt for many useful, stimulating discussions on this topic. This work was performed in part by the Lawrence Livermore National Laboratory under the auspices of the U. S. Department of Energy under Contract No. W-7405-ENG-48. This work was also sponsored in part by the Strategic Defense Initiative Organi-

zation, Office of Innovative Science and Technology, under the management of Harry Diamond Laboratories.

APPENDIX A: HERMITE-GAUSSIAN PULSES

Let space be restricted to real variable only. Then with the ansatz (2.1), the wave equation (2.2) reduces to the Schrödinger equation (2.3) without any source terms. In x,y coordinates this becomes

$$4ik\partial_\tau F_k+\partial_x^2 F_k+\partial_y^2 F_k=0 . \tag{A1}$$

One may obtain Hermite-Gaussian, exact solutions by performing the constructions given in any of the standard texts describing laser fields.[50,51] The difference between those approximate laser mode derivations and the following exact pulse solutions is the presence of the variables $\tau=z-ct$ and $\sigma=z+ct$ rather than just the spatial coordinate z alone. No second-order spatial derivatives are neglected here.

Let us assume

$$F_k(x,y,\tau)=\text{const}\times\exp[i(P(\tau)+k\rho^2/q(\tau))] .$$

Equation (A1) then yields two equations, one for q and one for P:

$$\partial_\tau q=+1 , \quad \partial_\tau P=+i/q .$$

The first equation gives

$$q=q_0+\tau=-iz_0+\tau . \tag{A2}$$

The second is satisfied by

$$-P=i\ln\left[\frac{w_0}{w(\tau)}\right]+\arctan(\tau/z_0) , \tag{A3}$$

if one sets

$$w(\tau)=\{w_0^2[1+(\tau/z_0)^2]\}^{1/2} , \tag{A4}$$

so that

$$\partial_\tau w=\left[\frac{w_0}{z_0}\right]^2\frac{\tau}{w(\tau)} .$$

In contrast with a conventional laser-beam field derivation, the beam-source location term z_0 is assumed here to be independent of the parameters k and w_0. Standard derivations would set $z_0=kw_0^2$.

The Hermite polynomials are now included in the solution in the usual manner. A difference from standard analyses also occurs here in the argument of the Hermite polynomials. If one sets

$$R(\tau)=\tau[1+(z_0/\tau)^2] , \tag{A5}$$

$$\eta(\tau)=-[(n+m)(z_0/kw_0^2)+1]\arctan(\tau/z_0) , \tag{A6}$$

$$\Omega(\tau)=(z_0/kw_0^2)w(\tau) , \tag{A7}$$

the real argument Hermite-Gaussian pulses take the form

$$\Phi_{nm}(x,y,\tau,\sigma;k)=\frac{w_0}{w(\tau)}H_n(\sqrt{2}x/\Omega(\tau))H_m(\sqrt{2}y/\Omega(\tau))\times\exp\left[-\frac{(x^2+y^2)}{\Omega^2(\tau)}\right]\exp\left[i\left[\frac{k(x^2+y^2)}{R(\tau)}+\eta(\tau)+k\sigma\right]\right] . \tag{A8}$$

With $n=m=0$, one has recovered, up to a constant multiplier, the fundamental Gaussian pulse (2.5):

$$\begin{aligned}\Phi_{00}(x,y,z,t;k)&=\frac{w_0}{w(\tau)}\exp\left[-\frac{(x^2+y^2)}{\Omega^2(\tau)}\right]\exp\left[i\left[\frac{k(x^2+y^2)}{R(\tau)}+\eta(\tau)+k\sigma\right]\right]\\&=e^{ik\sigma}e^{-i\arctan(\tau/z_0)}\frac{z_0}{(z_0^2+\tau^2)^{1/2}}\exp\left[-\frac{\rho^2}{(z_0/k)[1+(\tau/z_0)^2]}\right]\exp\left[i\frac{k\rho^2}{\tau[1+(z_0/\tau)^2]}\right]\\&=\frac{z_0}{z_0+i(z-ct)}e^{-k\rho^2/[z_0+i(z-ct)]}e^{ik(z+ct)} .\end{aligned} \tag{A9}$$

This result requires the identity

$$\begin{aligned}e^{-i\arctan(x)}&=\cos[\arctan(x)]-i\sin[\arctan(x)]\\&=(1-ix)/(1+x^2)^{1/2} .\end{aligned}$$

One can now proceed as with the superposition (2.6) to obtain EDEPT solutions and the spectrum (3.3) that led to the MPS pulse. Here one has explicitly accounted for the possibility of higher-order terms.

A comparison of (A8) with the expressions in Ref. 50, Secs. 6.6 and 6.9 or Ref. 51, Secs. 2.2 and 2.4, reveals only the differences noted above: the presence of the variables $\tau=z-ct$ and $\sigma=z+ct$ rather than just the spatial coordinate z alone. In fact, making the replacements $\sigma\to 2z$, $\tau\to z$, and $k\to k/2$, one reduces (A8) to the standard form. Although this derivation does not rely on the presence of a source term at a complex location, it reinforces the connections between the stationary-complex-source beam fields (laser modes) and the moving-complex-source beam fields (EDEPT laser pulses). The case for employing the complex-source location interpretations of the

beam fields to understand the underlying physics is also made stronger by these close analogies.

For $z_0 \equiv kw_0^2$, one obtains exact wave-equations solution counterparts of the real-argument Gaussian-Hermite laser beams introduced by Kogelnik and Li.[52] One can also generalize the complex-argument Gaussian-Hermite laser beams introduced by Siegman.[53] These solutions will be discussed in detail in Ref. 54.

APPENDIX B: FINITE ENERGY EDEPT'S

It will be shown in this appendix that the EDEPT representation (2.6) yields finite-energy solutions of the scalar wave equation (2.2) and of Maxwell's equations. First consider the general integral

$$I(x)=\int_{-\infty}^{\infty} g(ixy)dy \ , \tag{B1a}$$

where the function $g(z)$ is assumed to be analytic for $\mathrm{Re}(z)>-\epsilon$, $\epsilon>0$, and to have the following decay properties along an arc at infinity:

$$\lim_{R\to\infty}\left[R^{1+\epsilon}\int_{-\pi/2}^{\pi/2} g(\mathrm{Re}^{i\theta})e^{i\theta}d\theta\right]=0 \ . \tag{B1b}$$

Rewriting the integral (B1a) along the non-negative real axis yields

$$I(x)=\int_0^{\infty}[g(ixy)+g(-ixy)]dy \ .$$

Then with the rule for differentiating under an integral sign and a change of variables $u=|x|y$, one obtains

$$\begin{aligned} I(x)&=\frac{d}{dx}\int_0^{\infty} dy\frac{1}{y}\int_0^{xy} dt\,[g(it)+g(-it)] \\ &=\frac{d}{dx}\int_0^{\infty} du\frac{1}{u}\int_0^{\mathrm{sgn}(x)u} dt\,[g(it)+g(-it)] \ . \end{aligned}$$

Because of the symmetries of the integrand, the function $\mathrm{sgn}(x)$ can be removed from the limit of integration and differentiated to give

$$\begin{aligned} I(x)&=\frac{d}{dx}[\,\mathrm{sgn}(x)]\int_0^{\infty} du\frac{1}{u}\int_0^{u} dt\,[g(it)+g(-it)] \\ &=2\delta(x)\int_0^{\infty} du\frac{1}{u}\int_0^{u} dt\,[g(it)+g(-it)] \ . \end{aligned}$$

With an integration by parts, the assumed decay properties (B1b), and the definition of the complex logarithm function, one finally obtains

$$\begin{aligned} I(x)&=-2\delta(x)\int_0^{\infty} du\,\ln u\,[g(iu)+g(-iu)] \\ &=+2\delta(x)\int_0^{\infty} dz\,g(z)[i\ln(+iz)-i\ln(-iz)] \\ &=2\pi\delta(x)\int_0^{\infty} g(t)dt \ . \end{aligned} \tag{B2}$$

Let

$$g(t)=\frac{1}{(t+\Lambda)^{\mu}} \quad (\mu>1,\ \Lambda>0) \ . \tag{B3a}$$

With (B2) one then has

$$I(x)=\int_{-\infty}^{\infty} dy\frac{1}{(\Lambda+ixy)^{\mu}}=\frac{2\pi\delta(x)}{(\mu-1)\Lambda^{\mu-1}} \ . \tag{B3b}$$

This is a slight generalization of Hillion's result given in the appendix of Ref. 11. Similarly with (B2) and with Eq. 5.1.5 of Ref. 55, if

$$g(t)=\frac{e^{-t}}{(t+\Lambda)^m} \quad (m=1,2,\ldots;\Lambda>0) \ , \tag{B4a}$$

one also has

$$\begin{aligned} I_m(x;\Lambda)&=\int_{-\infty}^{\infty} dy\frac{e^{-ixy}}{(\Lambda+ixy)^m} \\ &=2\pi\delta(x)\frac{e^{\Lambda}}{\Lambda^{m-1}}\int_1^{\infty}\frac{e^{-\Lambda t}}{t^m}dt \\ &=2\pi\delta(x)\frac{e^{\Lambda}}{\Lambda^{m-1}}E_m(\Lambda) \ . \end{aligned} \tag{B4b}$$

Note that the exponential functions $E_n(x)$ have upper bounds given by Eqs. 5.1.19 and 5.1.20 or Ref. 55:

$$e^x E_1(x)<\ln\left[1+\frac{1}{x}\right] \quad (x>0) \ , \tag{B5a}$$

$$e^x E_n(x)\le\frac{1}{x+n-1} \quad (x>0;n=2,3,\ldots) \ . \tag{B5b}$$

Now consider the total energy of a scalar wave field. Since it can be written in the form

$$U_{\mathrm{tot}}=\int_{-\infty}^{\infty} dz\int_0^{\infty} d\rho\,\rho\int_0^{2\pi} d\theta\,|f|^2 \ ,$$

the total energy of the axisymmetric EDEPT solution (2.6) is

$$\begin{aligned} U_{\mathrm{tot}}&=\int_{-\infty}^{\infty} dz\int_0^{\infty} d\rho\,\rho\int_0^{2\pi} d\theta\left[\frac{1}{16\pi^2(z_0^2+\tau^2)}\int_0^{\infty} dk\,F(k)e^{-ks}\int_0^{\infty} dk'\,F^*(k')e^{-k's^*}\right] \\ &=\frac{1}{8\pi}\int_0^{\infty} dk\int_0^{\infty} dk'\,F(k)F^*(k')\int_{-\infty}^{\infty} dz\frac{1}{z_0^2+\tau^2}\int_0^{\infty} d\rho\,\rho e^{-(ks+k's^*)} \ , \end{aligned} \tag{B6}$$

where F^* and s^* are, respectively, the complex conjugates of F and s. Since

$$ks+k's^*=\rho^2\left[\frac{(k+k')z_0+i(k'-k)\tau}{z_0^2+\tau^2}\right]-i(k-k')\sigma \ ,$$

and

$$\frac{\rho}{z_0^2+\tau^2}e^{-(ks+k's^*)}=-\frac{1}{2}\frac{e^{i(k-k')\sigma}}{(k+k')z_0+i(k'-k)\tau}\partial_\rho\exp\left[-\left[\frac{(k+k')z_0+i(k'-k)\tau}{z_0^2+\tau^2}\right]\rho^2\right],$$

the energy (B6) becomes

$$U_{\rm tot}=\frac{1}{16\pi}\int_0^\infty dk\int_0^\infty dk'\,F(k)F^*(k')e^{-2i(k'-k)ct}\int_{-\infty}^{\infty}d\tau\frac{e^{-i(k'-k)\tau}}{(k+k')z_0+i(k'-k)\tau}\ . \tag{B6'}$$

The τ integration can be performed as a contour integral and with the help of (B4). Consider first the case where $k'\neq k$. The only pole of the integrand in the τ integration of (B6') occurs at

$$\tau_p=i\left[\frac{k+k'}{k'-k}\right]z_0\ .$$

Thus the sign of $(k'-k)$ determines whether τ_p is located in the upper or lower half of the complex τ plane. It is in the upper (lower) half-plane if $(k'-k)>0$ $[(k'-k)<0]$. However, to ensure the proper behavior at infinity of the integrand so that the contour can be closed in the upper (lower) half-plane, one must have $(k'-k)<0$ $[(k-k')>0]$. Consequently, because the pole is not contained within the closed contours, the τ integral is zero for $k'\neq k$. Now, to make use of (B2), assume that $k'=k+\xi$, where $\xi\ll 1$. The energy integral (B6') takes the form

$$U_{\rm tot}=\frac{1}{8\pi}\int_0^\infty dk\int_0^\infty dk'\,F(k)F^*(k')e^{-2i\xi ct}\times\int_{-\infty}^{\infty}d\tau\frac{e^{-i\xi\tau}}{2kz_0+i\xi\tau}\ .$$

With Eqs. (B4) and (B5) one has immediately

$$U_{\rm tot}=\frac{1}{4}\int_0^\infty dk\,|F(k)|^2e^{2kz_0}E_1(2kz_0)$$

$$<\frac{1}{4}\int_0^\infty dk\,|F(k)|^2\ln\left[1+\frac{1}{2kz_0}\right]$$

$$<\frac{1}{8z_0}\int_0^\infty dk|F(k)|^2\frac{1}{k}\ . \tag{B7}$$

Therefore, the EDEPT pulses will have finite energy if, at least, $F(k)/\sqrt{k}$ is square integrable. This is readily satisfied by MPS pulse since its spectrum (3.2) decays exponentially as $k\to\infty$ and is identically zero near $k=0$. However, the tighter logarithmic bound is needed for the splash pulse because its spectrum is constant at $k=0$. With Eqs. (4.331.1) and (4.337.1) of Ref. 56 the splash pulse spectrum gives

$$U_{\rm splash}<\int_0^\infty dk\,e^{-2ak}\ln\left[1+\frac{1}{2kz_0}\right]$$

$$=\frac{1}{8a}[\gamma+\ln(a/z_0)+e^{a/z_0}E_1(a/z_0)]\ ,$$

where Euler's constant $\gamma=0.577\,215\,7\ldots$. This bound is finite for $a>0$.

Now consider the electromagnetic-field-energy expression associated with the TE fields given by Eqs. (3.13):

$$U_{\rm EM}=\int_{-\infty}^{\infty}dz\int_0^\infty d\rho\,\rho\int_0^{2\pi}d\theta(\epsilon|E_\theta|^2+\mu|H_\rho|^2+\mu|H_z|^2)\ . \tag{B8}$$

Applying the operators directly to (2.6), one has the "bases functions" for the EM fields:

$$\tilde{E}_\theta(\mathbf{r},t;k)=Z_o\partial_\rho\partial_{ct}\Phi_k$$

$$=Z_0\left[-\frac{4ik\rho}{(z_0+i\tau)^2}+\frac{2ik^2\rho^3}{(z_0+i\tau)^3}-\frac{2ik^2\rho}{(z_0+i\tau)}\right]\Phi_k\ , \tag{B9a}$$

$$\tilde{H}_\rho(\mathbf{r},t;k)=\partial_z\partial_{ct}\Phi_k$$

$$=\left[+\frac{4ik\rho}{(z_0+i\tau)^2}-\frac{2ik^2\rho^3}{(z_0+i\tau)^3}-\frac{2ik^2\rho}{(z_0+i\tau)}\right]\Phi_k\ , \tag{B9b}$$

$$\tilde{H}_z(\mathbf{r},t;k)=4\partial_\tau\partial_\sigma\Phi_k$$

$$=4ik\left[-\frac{i}{(z_0+i\tau)}+\frac{ik\rho^2}{(z_0+i\tau)^2}\right]\Phi_k\ . \tag{B9c}$$

For instance, the field component

$$E_\theta(\mathbf{r},t)=\int_0^\infty dk\,F(k)\tilde{E}_\theta(\mathbf{r},t;k)\ .$$

The energy expression (B8) now becomes

$$U_{\rm EM}=\frac{1}{8\pi}\int_0^\infty dk\int_0^\infty dk'\,F(k)F^*(k')e^{-i(k'-k)ct}\int_{-\infty}^{\infty}dz\,e^{-i(k'-k)z}\int_0^\infty d\rho\,\rho e^{-[(k+k')z_0+i(k'-k)\tau]\rho^2/(z_0^2+\tau^2)}$$
$$\times\left[\frac{8k^2(k')^2\rho^7}{(z_0^2+\tau^2)^4}+\frac{16k^2(k')^2\rho^5}{(z_0^2+\tau^2)^3}+\frac{8k^2(k')^2\rho^3}{(z_0^2+\tau^2)^2}+\frac{32kk'\rho^3}{(z_0^2+\tau^2)^3}-\frac{16k(k')^2\rho^5}{(z_0^2+\tau^2)^3(z_0-i\tau)}\right.$$
$$\left.-\frac{16k^2k'\rho^5}{(z_0^2+\tau^2)^3(z_0+i\tau)}+\frac{16kk'\rho}{(z_0^2+\tau^2)^2}-\frac{16k(k')^2\rho^3}{(z_0^2+\tau^2)^2(z_0-i\tau)}-\frac{16k^2k'\rho^3}{(z_0^2+\tau^2)^2(z_0+i\tau)}\right].$$

With the integral (3.461.3) of Ref. 56,

$$\int_0^\infty dx\,x^{2m+1}e^{-ax^2}=\frac{m!}{2a^{m+1}},$$

the ρ integrations are readily done and after some algebraic manipulations one obtains

$$U_{\rm EM}=\frac{1}{2\pi}\int_0^\infty dk\int_0^\infty dk'\,k^2F(k)(k')^2F^*(k')e^{-i2(k'-k)ct}$$
$$\times[6I_4(k'-k;(k+k')z_0)+4I_3(k'-k;(k+k')z_0)+I_2(k'-k;(k+k')z_0)],$$

where I_m is given by (B4b). Proceeding as in the scalar case,

$$U_{\rm EM}=\int_0^\infty dk\,|F(k)|^2k^4e^{2kz_0}\left[6\frac{E_4(2kz_0)}{(2kz_0)^3}+4\frac{E_3(2kz_0)}{(2kz_0)^2}+\frac{E_2(2kz_0)}{2kz_0}\right].$$

With the recurrence relation 5.1.14 of Ref. 55,

$$E_{n+1}(z)=\frac{1}{n}[e^{-z}-zE_n(z)], \tag{B10}$$

This expression reduces to the form

$$U_{\rm EM}=\int_0^\infty dk\,|F(k)|^2k^4\left[\frac{2}{(2kz_0)^3}+\frac{1}{(2kz_0)^2}\right]$$
$$=\frac{1}{4z_0^4}\int_0^\infty dk\,|F(k)|^2[kz_0+(kz_0)^2]. \tag{B8'}$$

Therefore the EDEPT EM field is finite if $\int_0^\infty dk\,|F(k)|^2k^m<\infty$ for $m=1,2$. Since their spectra tend to constants as $k\to0$ and decay exponentially as $k\to\infty$, the splash and MPS pulses satisfy these constraints and, as a result, the associated electromagnetic fields have finite energy. In particular, the total energy in the electromagnetic MPS pulse is

$$U_{\rm EM}^{\rm MPS}\frac{16\pi^2\beta^2}{4z_0^4}e^{2ba}\int_{b/\beta}^\infty dk\,e^{-(2\beta a)k}[kz_0+(kz_0)^2]. \tag{B11}$$

With (3.351.2) of Ref. 56,

$$\int_y^\infty x^ne^{-\Lambda x}dx=e^{-\Lambda x}\sum_{j=0}^{n}\frac{n!}{j!}\frac{y^j}{\Lambda^{n-j+1}}, \tag{B12}$$

this expression becomes

$$U_{\rm EM}^{MPS}=\frac{\pi^2}{\beta z_0^4a^3}[1+2ba+2(ba)^2]. \tag{B11'}$$

[1]J. N. Brittingham, J. Appl. Phys. **54**, 1179 (1983).
[2]R. W. Ziolkowski, J. Math. Phys. **26**, 861 (1985).
[3]P. A. Belanger, J. Opt. Soc. Am. A **1**, 723 (1984).
[4]A. Sezginer, J. Appl. Phys. **57**, 678 (1985).
[5]P. A. Bélanger, J. Opt. Soc. Am. A **3**, 541 (1986).
[6]T. T. Wu and R. W. P. King, J. Appl. Phys., **56**, 2567 (1984).
[7]R. W. Ziolkowski, in Abstracts of the Proceedings of the Joint IEEE Antennas and Propagation Society and International Union of Radio Science Symposium, Blacksburg, VA, 1987 (unpublished), p. 168.
[8]R. W. Ziolkowski and E. Heyman, in Abstracts of the Proceedings of the XXII General Assembly of the International Union of Radio Science, Tel Aviv, Israel, 1987 (unpublished), p. 254.
[9]R. W. Ziolkowski, in *Proceedings of the SPIE Conference 873 on Microwave and Particle Beam Sources and Propagation,* Los Angeles 1988 (Society of Photo-Optical Instrumentation Engineers, Bellingham, WA, 1988), pp. 312–319.
[10]R. W. Ziolkowski (unpublished).
[11]P. Hillion, J. Appl. Phys. **60**, 2981 (1986).
[12]P. Hillion, J. Math. Phys. **28**, 1743 (1987).
[13]T. T. Wu, J. Appl. Phys. **57**, 2370 (1985).
[14]T. T. Wu, R. W. P. King, and H.-M. Shen, J. Appl. Phys. **62**, 4036 (1987).
[15]H.-M. Lee, Radio Sci. **22**, 1102 (1987).
[16]H.-M. Shen, Ref. 9, pp. 338–346.
[17]H.-M. Lee, Ref. 7, p. 174.
[18]J. A. Stratton, *Electromagnetic Theory* (McGraw-Hill, New York, 1941), pp. 360–361.
[19]A. G. van Nie, Philips Res. Rep. **19**, 378 (1964).
[20]P. M. Morse and H. Feshbach, *Methods of Theoretical Physics* (McGraw-Hill, New York, 1953), Vol. I, Chap. 7.

[21]J. Durnin, J. Opt. Soc. Am. A **4**, 651 (1987).
[22]J. Durnin, J. J. Miceli, Jr., and J. H. Eberly, Phys. Rev. Lett. **58**, 1499 (1987).
[23]D. DeBeer, S. R. Hartmann, and R. Friedberg, Phys. Rev. Lett. **59**, 2611 (1987).
[24]H. E. Moses and R. T. Prosser, IEEE Trans. Antennas Propag. **AP-34**, 188 (1986).
[25]H. E. Moses, J. Math. Phys. **25**, 1905 (1984).
[26] E. Heyman and L. P. Felsen, IEEE Trans. Antennas Propag. **AP-34**, 1062 (1986).
[27]E. Heyman and B. Z. Steinberg, J. Opt. Soc. Am. A **4**, 473 (1987).
[28]P. D. Einziger and S. Raz, J. Opt. Soc. Am. A **4**, 3 (1987).
[29]E. Heyman, B. Z. Steinberg, and L. P. Felsen, J. Opt. Soc. Am. A **4**, 2081 (1987).
[30]L. P. Felsen and E. Heyman, Ref. 9, pp. 320–328.
[31]G. A. Deschamps, Electron. Lett. **7**, 684 (1971).
[32]L. P. Felsen, Symp. Math. **18** (1976).
[33]L. P. Felsen, J. Opt. Soc. Am. **66**, 751 (1976).
[34]S. Y. Shin and L. P. Felsen, J. Opt. Soc. Am. **67**, 699 (1977).
[35]L. P. Felsen, J. Opt. Soc. Am. A **3**, 486 (1986).
[36]A. L. Cullen, F. R. S., and P. K. Yu, Proc. R. Soc. London, Ser. A **366**, 155 (1979).
[37]K. M. Luk and P. K. Yu, IEE Proc.-J. Optoelectron. **132**, part J, 105 (1985).
[38]K. M. Luk and P. K. Yu, IEE Proc.-J. Optoelectron. **132**, part J, 191 (1985).
[39]A. Trautman, Proc. R. Soc. London, Ser. A **270**, 326 (1962).
[40]E. T. Newman, J. Math. Phys. **14**, 102 (1973).
[41]A. Das, J. Math. Phys. **7**, (1966).
[42]I. M. Besieris, A. M. Shaarawi, and R. W. Ziolkowski, J. Math. Phys. (to be published).
[43]D. S. Jones, *The Theory of Electromagnetism* (Pergamon, New York, 1964), pp. 40–42.
[44]R. W. Ziolkowski, D. K. Lewis, and B. D. Cook, Phys. Rev. Lett. (to be published).
[45]A. M. Shaarawi, I. M. Besieris, and R. W. Ziolkowski, J. Appl. Phys. (to be published).
[46]M. Lax, W. Louisell, and W. McKnight, Phys. Rev. A **11**, 1365 (1975).
[47]R. W. Ziolkowski, A. M. Shaarawi, and I. M. Besieris, in Proceedings of the International Symposium on Spacetime Symmetries, College Park, MD, 1988 [Nucl. Phys. B (to be published)].
[48]T. Takenaka, M. Yokota, and O. Fukumitsu, J. Opt. Soc. Am. A **2**, 826 (1985).
[49]E. Zauderer, J. Opts. Soc. Am. A **3**, 465 (1986).
[50]A. Yariv, *Quantum Electronics,* 2nd ed. (Wiley, New York, 1975).
[51]A. Yariv and P. Yeh, *Optical Waves in Crystals* (Wiley, New York, 1984).
[52]H. Kogelnik and T. Li, Proc. IEEE, **54**, 312 (1966).
[53]A. E. Siegman, J. Opt. Soc. Am **63**, 1093 (1973).
[54]R. W. Ziolkowski (unpublished).
[55]*Handbook of Mathematical Functions,* edited by M. Abramowitz and I. A. Stegun (Dover, New York, 1965).
[56]I. S. Gradshteyn and I. M. Ryzhik, *Table of Integrals, Series, and Products* (Academic, New York, 1965).